



# Highly efficient electrocatalytic hydrogen evolution coupled with upcycling of microplastics in seawater enabled via $\text{Ni}_3\text{N}/\text{W}_5\text{N}_4$ janus nanostructures

Fahao Ma<sup>a</sup>, Shuhua Wang<sup>b</sup>, Xueqin Gong<sup>a</sup>, Xiaolei Liu<sup>a</sup>, Zeyan Wang<sup>a</sup>, Peng Wang<sup>a</sup>, Yuanyuan Liu<sup>a</sup>, Hefeng Cheng<sup>a</sup>, Ying Dai<sup>b</sup>, Zhaoke Zheng<sup>a,\*</sup>, Baibiao Huang<sup>a,\*</sup>

<sup>a</sup> State Key Laboratory of Crystal Materials, Shandong University, Jinan 250100, P. R. China

<sup>b</sup> School of Physics, Shandong University, Jinan 250100, P. R. China

## ARTICLE INFO

### Keywords:

Hydrogen evolution reaction  
Microplastics upgrading  
Value-added chemicals  
Metal nitrides-inducing growth  
 $\text{Ni}_3\text{N}/\text{W}_5\text{N}_4$  Janus nanostructure

## ABSTRACT

Electrochemical hydrogen evolution reaction (HER) coupled with microplastics reforming are critical for marine energy and environmental engineering, but filled with challenges. Herein,  $\text{Ni}_3\text{N}/\text{W}_5\text{N}_4$  Janus nanostructure with barrier-free heterointerface was designed via transition metal nitrides-inducing growth strategy. Benefiting from the interface synergistic effect, super-hydrophilic surface and multilevel Janus structure,  $\text{Ni}_3\text{N}/\text{W}_5\text{N}_4$  electrode displays Pt-like HER performance and the outstanding stability ( $\sim 300$  h) under industrially current. Meanwhile,  $\text{Ni}_3\text{N}/\text{W}_5\text{N}_4$  also exhibits high activity and selectivity toward electro-reforming of plastics, showing an ultralow overpotential of 1.33 V ( $\eta_{10}$ ) and generating the value-added HCOOH with the high Faradic efficiency of  $\sim 85\%$ . Impressively, driven by solar panels, the bifunctional  $\text{Ni}_3\text{N}/\text{W}_5\text{N}_4$  electrocatalyst achieves the highly efficient production of  $\text{H}_2$  and HCOOH ( $\eta_{10} = 1.4$  V,  $\eta_{\text{solar to hydrogen}} = 16.04\%$ ) in seawater full of plastics. This work underlines the on-site upgrading of plastic wastes and energy-saving hydrogen evolution in seawater enabled by the design of Janus heterostructures for metal nitrides.

## 1. Introduction

Plastics, especially for Poly (EthyleneTerephthalate) (PET), play an important and irreplaceable role in today's life [1]. Up to now, humans have produced about 900 million tons of plastics, and it is estimated that, the global production of plastics will reach 800 million tons per year after 2040 [2]. Unfortunately, along with people's excessive use of plastics, plastic pollution has seriously threatened the ecological environment and biological safety [3,4]. Especially, the microplastic fragments have been detected in the deepest ocean, which is very likely to invade some natural organisms and even human body through biological circulation [5,6]. Therefore, how to degrade and recycle these plastic wastes has become a hot topic of current research.

In the past years, plastic recycling technologies mainly include traditional physical and chemical recycling (Scheme 1a) [7]. The physical recycling technology has simple and low-cost process, but it has problems caused by additives and pollutants in plastics, which greatly limits its scope of application. For traditional chemical recycling, although it could reproduce plastics with the similar quality to original plastics, the high energy consumption and emission of greenhouse gases

make it difficult to achieve sustainable applications [8]. Recently, the upgrading of plastics, transformation from plastic waste to value-added chemicals, has provided a new promising pathway for recycling plastics [9]. For examples, Scott et al. proposed a series of hydrogenolysis/aromatization reaction of polyethylene under the catalysis of  $\text{Pt}/\gamma\text{-Al}_2\text{O}_3$ , which can directly convert waste polyethylene plastics into valuable alkyl aromatics and alkyl cycloalkanes [10]. Xie et al. realized the highly selective conversion of various waste plastics into  $\text{C}_2$  fuels via two steps based on photocatalysis technique [11]. Although some progress has been made in upcycling and degradation of plastics, these reforming processes often require harsh experimental conditions (high temperature and high pressure), and the overall efficiency is still not satisfied for its poor selectivity toward a single valuable chemical product [12,13].

In contrast, electrochemical plastics reforming is expected to offer a green, convenient and efficient plastics recycling pathway (Scheme 1b) [14]. On the one hand, electricity could be acquired from renewable energy sources, and the reaction conditions are relatively mild. On the other hand, the value-added chemicals generated from plastic upgrading on the anode could be coupled with the hydrogen production on the

\* Corresponding authors.

E-mail addresses: [zkzheng@sdu.edu.cn](mailto:zkzheng@sdu.edu.cn) (Z. Zheng), [bbhuang@sdu.edu.cn](mailto:bbhuang@sdu.edu.cn) (B. Huang).

<https://doi.org/10.1016/j.apcatb.2022.121198>

Received 15 December 2021; Received in revised form 29 January 2022; Accepted 7 February 2022

Available online 10 February 2022

0926-3373/© 2022 Elsevier B.V. All rights reserved.

counter electrode simultaneously [15,16]. More importantly, in consideration of the widespread pollution of plastics, especially the microplastics in seawater, the highly efficient electro-reforming of microplastics coupled with the hydrogen evolution reaction (HER) is of great significance for marine energy and environmental engineering [17]. This field, however, is currently still a huge blank. To achieve this goal, the catalysts need to efficiently drive HER process and meet the requirements of high activity and selectivity toward plastic upgrading. Meanwhile, the excellent resistance to chloride ion corrosion from seawater is also the crucial premise for catalysts [18].

Recently, two-dimensional (2D) transition metal nitrides (TMNs), such as W-N, Mo-N are promising candidates for energy-related electrocatalysis because of their inherent characters, including high resistant of corrosion, electrical conductivity and tunable electronic structure [19]. Nevertheless, the fabrication of these 2D TMNs is limited by the tedious and time-consuming salt template method, and the prepared 2D TMNs are typically N-rich [20]. Owing to the weak overlap of atomic wave functions, the N-rich TMNs exhibit strong interaction between N sites and  $H_{ad}$ , and thus do not behave as expected toward HER [21]. Therefore, it is urgent to explore the new method of preparing 2D TMNs with appropriate atom ratio of metal versus to N. Furthermore, the multilevel nanostructures, comprised of 2D and 3D structure, usually exhibit large specific surface area and excellent mass transfer capability. Particularly, the 3D  $Ni_3N$  NPs possess appropriate  $\Delta G^*_{H}$ , and hence the strong mutual interaction or synergistic effect may generate at heterointerface [22–24]. However, most of reported heterointerface forms schottky or p-n junctions, which has unidirectional conductive rectification characteristics, and hence are not suitable to drive effectively both anodic reaction and cathodic reaction, simultaneously [25,26]. Therefore, the establishment of a functionally complementary and non-interface barrier heterostructure is critical for construct bifunctional catalysts accomplishing the highly efficient HER and plastics upgrading in seawater [27–31].

Herein, the on-site upgrading of microplastics coupled with hydrogen evolution in seawater via electrocatalysis were firstly reported in our work. The highly efficient bifunctional electrode of  $Ni_3N/W_5N_4$  with Janus nanostructure and barrier-free heterointerface was designed via transition metal nitrides-inducing growth strategy. Systematical studies reveal that the presence of transition metal nitrides ( $Ni_3N$ ,  $Co_4N$  and  $Fe_4N$ ) are critical for enabling the formation of special  $W_5N_4$  hexagonal phase and Janus heterointerface. Simultaneously, the 2D  $W_5N_4$

nanosheets exhibit strong confinement effect, which significantly limit the size of  $Ni_3N$  particles. Experimental and theoretical results indicate that, owing to the multilevel sponge-like structure and the synergistic effect at heterointerface, the  $Ni_3N/W_5N_4$  Janus nanostructure displays Pt-like HER activity in both deionized water and seawater. Impressively, the  $Ni_3N/W_5N_4$  electrode shows unprecedented stability under industrially current for  $\sim 300$  h. More interestingly, the electro-reforming of plastic could also be effectively performed over the  $Ni_3N/W_5N_4$  Janus nanostructure, and the overpotential ( $\eta_{10}$ ) is greatly reduced by  $\sim 210$  mV compared to that of OER, reaching an ultralow potential of  $\sim 1.33$  V. Furthermore, the Faradic efficiency of  $HCOOH$  production is as high as 85% at large current of  $120 \text{ mA cm}^{-2}$ , indicating the high selectivity toward plastics upgrading. To our surprised, chlorine evolution reaction (CER) process, the main bottleneck for seawater splitting, will be largely inhibited during the PET upcycling process, which in return enlarged the safe voltage window. Finally, in view of the excellent performance of  $Ni_3N/W_5N_4$  toward HER and plastics upgrading, we assembled it into a solar-driven and membrane-free electrolysis device, which exhibits an ultra-low overpotential of 1.4 V to reach 10 mA, demonstrating the promising application for energy-saving  $H_2$  production and waste plastics degradation in seawater.

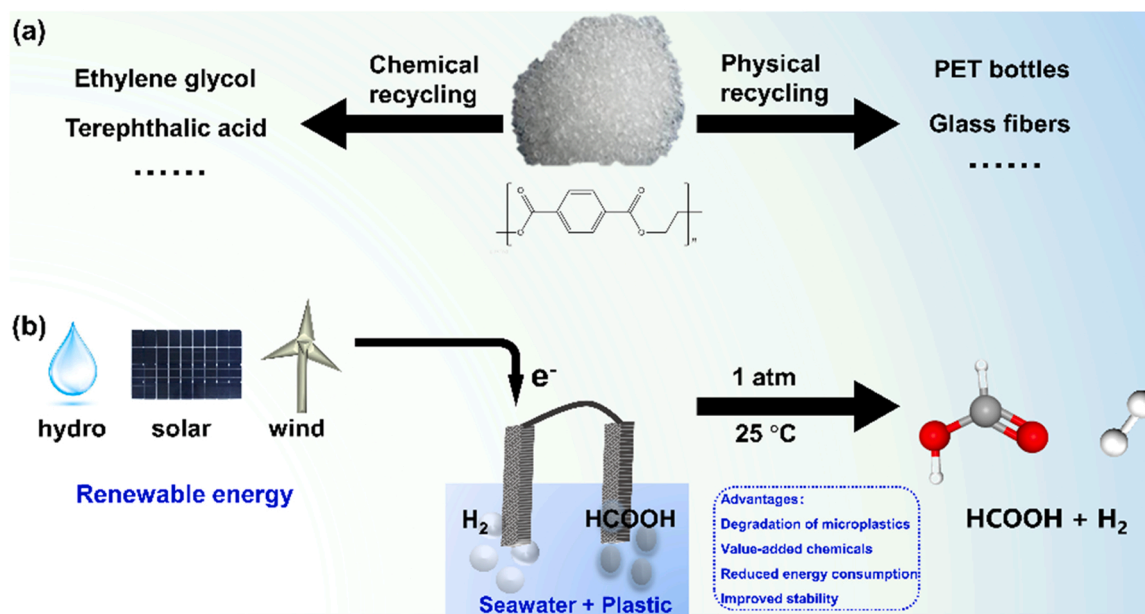
## 2. Experimental

### 2.1. Chemicals

Nickel nitrate hexahydrate ( $Ni(NO_3)_2 \cdot 6 H_2O$ ), Ferric nitrate nonahydrate ( $Fe(NO_3)_3 \cdot 9 H_2O$ ), Cobaltous Nitrate Hexahydrate ( $Co(NO_3)_2 \cdot 6 H_2O$ ), ammonium fluoride ( $NH_4F$ ) and urea ( $CH_4N_2O$ ) were purchased from Sinopharm Chemical Reagent. Ammonium tungsten partial ( $H_{28}N_6O_{41}W_{12}$ ) and Polyethylene Terephthalate (PET ( $C_{10}H_8O_4$ ))<sub>n</sub>) were obtained from Alfa Aesar. All these reagents were used without further purification and all the standard solutions were prepared with Milli-Q water.

### 2.2. Synthesis of Ni-OH nanosheets

The Ni-OH nanosheets grown on Ni foam were synthesized via hydrothermal method. Specifically, 0.581 g of  $Ni(NO_3)_2 \cdot 6 H_2O$ , 0.185 g of  $NH_4F$  and 0.6 g of  $CH_4N_2O$  were added into 35 mL of deionized water. In order to form a homogeneous solution, the stirring process was



**Scheme 1.** (a) Traditional method for PET recycling including chemical recycling and physical recycling. (b) Upgrading of PET via electrocatalysis.

performed for 10 min. Then, the solutions was transferred into the reactor with a cleaned Ni foam (NF,  $2 \times 4 \text{ cm}^2$ ), and maintained  $120^\circ\text{C}$  for 6 h.

### 2.3. Preparation of 3D sponge-like NiW-OH nanostructure

The NiW-OH nanosheets were synthesized via ion exchange strategy. In detail, 0.125 mmol of  $\text{H}_{28}\text{N}_6\text{O}_{41}\text{W}_{12}$  were put into 50 mL Teflon-lined stainless-steel autoclave with 35 mL of deionized water, and the prepared Ni-OH@NF. Then, the autoclave was maintained at  $180^\circ\text{C}$  for 12 h.

### 2.4. Preparation of $\text{Ni}_3\text{N}/\text{W}_5\text{N}_4$ Janus nanostructure and $(\text{Co}/\text{Fe})_4\text{N}-\text{W}_5\text{N}_4$ Janus nanostructure

The  $\text{Ni}_3\text{N}-\text{W}_5\text{N}_4$  Janus nanostructure was obtained via nitridation engineering. The prepared NiW-OH nanostructure electrode was placed in a porcelain boat, and then put into the central of tubular furnace. Afterwards, the temperature of furnace was evaluated to  $600^\circ\text{C}$  with a heating rate of  $5^\circ\text{C}/\text{min}$  under  $\text{NH}_3$  atmosphere and maintained for 2 h. In order to explore the effect of temperature toward activity, the samples were also prepared at different temperature ( $450^\circ\text{C}$ ,  $500^\circ\text{C}$ ,  $550^\circ\text{C}$ ,  $650^\circ\text{C}$  and  $700^\circ\text{C}$ , respectively).

In addition, the  $(\text{Co}/\text{Fe})_4\text{N}-\text{W}_5\text{N}_4$  Janus nanostructures were also synthesized via the similar method as  $\text{Ni}_3\text{N}-\text{W}_5\text{N}_4$  Janus nanostructure. Firstly,  $\text{Co}(\text{NO}_3)_2 \cdot 6\text{H}_2\text{O}$  or  $\text{Fe}(\text{NO}_3)_3 \cdot 9\text{H}_2\text{O}$ , 0.185 g of  $\text{NH}_4\text{F}$  and 0.6 g of  $\text{CH}_4\text{N}_2\text{O}$  were added into 35 mL of deionized water to form a homogeneous solution. Then, to form the Co-OH or Fe-OH precursors grown on Ni foam, the solutions were transferred into the reactor with a cleaned Ni foam, and maintained  $120^\circ\text{C}$  for 6 h. Subsequently, the CoW-OH or FeW-OH precursors were prepared via ion exchange strategy. In detail, 0.125 mmol of  $\text{H}_{28}\text{N}_6\text{O}_{41}\text{W}_{12}$  were put into 50 mL Teflon-lined stainless-steel autoclave with 35 mL of deionized water and the prepared Co-OH@NF or Fe-OH@NF, and the autoclave was maintained at  $180^\circ\text{C}$  for 12 h. Lastly, the  $(\text{Co}/\text{Fe})_4\text{N}-\text{W}_5\text{N}_4$  Janus nanostructure was obtained through nitridation strategy, and the heating condition is the same as  $\text{Ni}_3\text{N}-\text{W}_5\text{N}_4$  Janus structure.

### 2.5. Preparation of $\text{W}_5\text{N}_4$ nanosheets

To obtain the pure phase of hexagonal  $\text{W}_5\text{N}_4$ , the chemical dealloying process through nitric acid (10 wt%) was performed toward  $\text{Ni}_3\text{N}/\text{W}_5\text{N}_4$  hybrid structure.

### 2.6. Preparation of the cubic phase of WN

The cubic phase of WN was synthesized via direct nitridation engineering of the ammonium tungsten partial, and the temperature of furnace was evaluated to  $600^\circ\text{C}$  with a heating rate of  $5^\circ\text{C}/\text{min}$  under  $\text{NH}_3$  atmosphere and maintained for 2 h.

### 2.7. Preparation of $\text{Ni}_3\text{N}-\text{W}_5\text{N}_4$ heterostructure (without template)

Firstly, to obtain NiW-precursor (without template), 0.125 mmol of  $\text{H}_{28}\text{N}_6\text{O}_{41}\text{W}_{12}$  and 2 mmol of  $\text{Ni}(\text{NO}_3)_2 \cdot 6\text{H}_2\text{O}$  were dissolved into 35 mL of water. Then, the solution was put into 50 mL Teflon-lined stainless-steel autoclave with a cleaned Ni foam (NF,  $2 \times 4 \text{ cm}^2$ ), and maintained at  $180^\circ\text{C}$  for 10 h. Subsequently, the as-prepared NiW-precursor was gone through nitride process at  $600^\circ\text{C}$  for 2 h, and then the  $\text{Ni}_3\text{N}-\text{W}_5\text{N}_4$  heterostructure (without template) formed.

### 2.8. Characterization

Powder X-ray diffraction (XRD) analysis was carried out via the Bruker D8ADVANCE powder diffractometer with Cu K $\alpha$  X-ray radiation. The morphology characters of these samples were investigated by

scanning electron transmission microscopy (SEM) images (Hitachi S-4800 microscope) and transmission electron microscopy (TEM) (JEOL JEM-2100 F). The STEM images and energy-dispersive X-ray spectroscopy (EDX) were also performed on JEOL JEM-2100 F. The chemical environment of the samples was characterized by X-ray photoelectron spectroscopy (XPS) (Thermo ESCALAB 250XI) and Ultraviolet photoelectron spectroscopy (UPS) (Thermo ESCALAB 250XI PHI5000 Versa Probe III). The static water contact-angle measurements were performed via Theta Flex. The Brunauer-Emmett-Teller (BET) surface areas was obtained via Kubo X1000. The gas chromatograph equipped with a TDX-01 column with a flame ionization detector and a  $\text{H}_2$ -detection GC (shiweipxGC-7806) was used to analyze the amount of  $\text{H}_2$ .

### 2.9. Electrochemical measurements

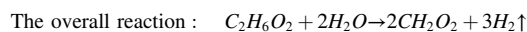
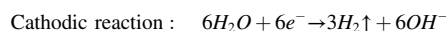
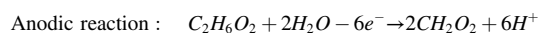
All the electrochemical measurements were performed on the CHI 750E electrochemical workstation. A typical three-electrode system was applied in our experiments to evaluate the corresponding HER and PET upgrading activity, selectivity and stability. Specifically, a Hg/HgO electrode and graphite rod were used as the counter and the reference electrode, respectively, and the prepared catalyst with the electrode area of  $1 \text{ cm}^2$  was selected as the working electrode. The measured potentials versus the reversible hydrogen electrode (RHE) were converted according to the equation:  $E_{\text{RHE}} = E_{\text{Hg}/\text{HgO}} + 0.099 + 0.0592 \times \text{pH}$ . The linear sweep voltammetry (LSV) curves were measured at a scan rate of  $5 \text{ mV s}^{-1}$  and the potential were not corrected (without iR compensation). The double-layer capacitance ( $C_{\text{dl}}$ ) via cyclic voltammograms (CV) at different scan rates were measured to investigated electrochemically active surface areas (ECSA). The CV was measured in the potential range from 0.05 to 0.15 V vs RHE at different scan rate. Electrochemical impedance spectroscopy (EIS) was measured with 5 mV amplitude in a frequency range from  $10^5$  to 0.01 Hz. The stability of HER and PET upgrading for catalyst was investigated via chronoamperometric (i-t) response tests. A two-electrode system were assembled to evaluate the capability of electrochemical plastic reforming coupling HER.

### 2.10. The preparation of PET lysate

First, 2.0 g of PET flakes originated from cutting commercially available PET bottle were soaked in 100 mL deionized water and seawater with 0.4 mol KOH, respectively. In order to dissolve all the plastic in the alkaline solution, the temperature of these solutions maintain  $80^\circ\text{C}$  for 48 h. Subsequently, another 300 mL deionized water or seawater were put into original solution to form the PET solution. Lastly, the formed 1 M KOH solution of 100 mL (deionized water or seawater) with PET lysate were directly used for HER and PET reforming process. The main composition of PET lysate includes ethylene glycol and terephthalic acid.

### 2.11. Quantitative oxidative product analysis

The  $\text{H}_2$  products was characterized by a gas chromatograph equipped with a TDX-01 column with a flame ionization detector and a  $\text{H}_2$ -detection GC (shiweipxGC-7806). The liquid production was analyzed via Nuclear Magnetic Resonance Spectrometer (NMR, AVANCE NEO 400 MHz). The relevant Faradic efficiency was calculated according to the following reaction equation.



For plastics upgrading reaction,

$$\text{For HER, Faradic efficiency (\%)} = \frac{\text{mol of formed } H_2 \times 2F}{\text{total passed charge}} \times 100\%$$

$$\text{Faradic efficiency (\%)} = \frac{\text{mol of formed } CH_2O_2 \times 3F}{\text{total passed charge}} \times 100\%$$

## 2.12. Theoretical calculation

Density functional theory calculations were performed using Vienna ab initio simulation package. Projector augmented wave potentials [32–34] and Perdew-Burke-Ernzerhof (PBE) functional within the generalized gradient approximation (GGA) [35] were considered in the calculation. For the structural optimization of bulk  $Ni_3N$ ,  $W_5N_4$  and WN, the cutoff energy was set to be 500 eV, and the  $k$ -point sampling grid for bulk  $Ni_3N$ ,  $W_5N_4$  and WN are  $8 \times 8 \times 6$ ,  $6 \times 6 \times 2$  and  $6 \times 6 \times 6$ . And, the optimized lattice parameters of the bulk  $Ni_3N$  ( $a = b = 4.601 \text{ \AA}$ ,  $c = 4.294 \text{ \AA}$ ),  $W_5N_4$  ( $a = b = 2.887 \text{ \AA}$ ,  $c = 4.294 \text{ \AA}$ ) and WN ( $a = b = c = 4.367 \text{ \AA}$ ) are in good agreement with experimental values. Then, we were built  $Ni_3N$  (002) surfaces,  $W_5N_4$  (002) surfaces and  $W_5N_4$  (100) surfaces. The convergence tolerances of energy and force is set  $1.0 \times 10^{-5} \text{ eV/atom}$  and  $1.0 \times 10^{-2} \text{ eV/\AA}$ . The vacuum space along the  $z$

direction is set to be  $15 \text{ \AA}$ . Moreover, the DFT-D2 method is used to describe van der Waals interaction in this work [36]. The diffusion decomposition of  $H_2O$  was determined by climbing image-nudged elastic band (CI-NEB) [37].

The adsorption energy ( $E_{\text{abs}}$ ) of  $H_2O$  on  $Ni_3N$  and  $W_5N_4$  can be written as:

$$E_{\text{abs}} = E(\text{sub} + H_2O) - E(\text{sub}) - E(H_2O)$$

$E(\text{sub} + H_2O)$  is the total energy of the system after  $H_2O$  is adsorbed on the surface of  $Ni_3N$  or  $W_5N_4$ .  $E(\text{sub})$  is the total energy of  $Ni_3N$  or  $W_5N_4$  surfaces.  $E(H_2O)$  is the total energy of  $H_2O$ .

The Gibbs free energy change ( $\Delta G$ ) of the elementary step is calculated by:

$$\Delta G = \Delta E + \Delta E_{\text{ZPE}} - T\Delta S$$

Where  $\Delta E$  represents the total energy difference,  $\Delta E_{\text{ZPE}}$  and  $\Delta S$  were the change in the zero-point energy and the entropy, respectively.

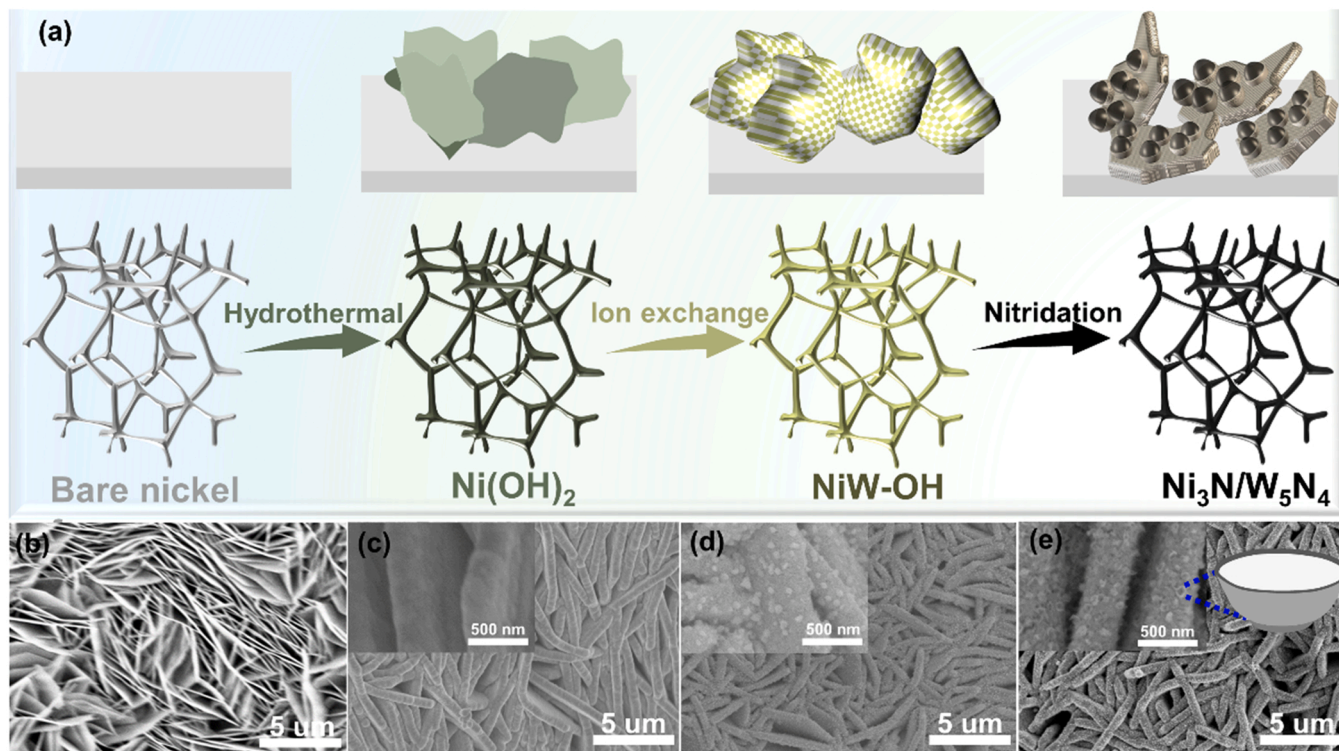


**Fig. 1.** Schematic formation process and morphological characterizations. (a) The schematic illustration of constructing the  $Ni_3N/W_5N_4$  electrode with Janus nanostructures. (b-e) SEM images of Ni-OH, NiW-OH,  $Ni_3N/W_5N_4$  and  $W_5N_4$ , respectively.



### 3. Results and discussion

#### 3.1. Synthesis and characterizations of $\text{Ni}_3\text{N}/\text{W}_5\text{N}_4$ Janus structure

The  $\text{Ni}_3\text{N}/\text{W}_5\text{N}_4$  Janus nanostructure was prepared via a simple three-steps method, including hydrothermal process, ions exchange and nitridation engineering (Fig. 1a). In detail, the Ni-OH precursors were directly grown on Ni foam through a facile hydrothermal process (Fig. 1b). Then, the three-dimensional (3D) sponge-like NiW-OH nanostructure was synthesized via ions exchange strategy (Fig. 1c) and the corresponding X-ray diffraction (XRD) patterns shows the phase transformation from Ni-OH to NiW-OH precursors (Fig. S1). Finally, the  $\text{Ni}_3\text{N}/\text{W}_5\text{N}_4$  heterostructure were obtained upon the nitridation engineering under the atmosphere of  $\text{NH}_3$ . As shown in Fig. 1d, the 3D sponge-like nanostructure of NiW-OH precursors can be well inherited after nitridation process. The high-resolution scanning electron microscopy (SEM) image (the inset of Fig. 1d) and XRD spectrum (Fig. S2) exhibit that these sponge-like networks are self-assembled by  $\text{W}_5\text{N}_4$  ultra-thin nanosheets and  $\text{Ni}_3\text{N}$  nanoparticles (NPs) with a mean diameter of  $\sim 50$  nm. It is noteworthy that, due to the spatial confinement effect, the growth and aggregation of  $\text{Ni}_3\text{N}$  nanoparticles were largely weakened compared to that without the existence of  $\text{W}_5\text{N}_4$  (Fig. S3). Furthermore, to obtain the pure phase of hexagonal  $\text{W}_5\text{N}_4$ , the chemical dealloying process through nitric acid (10 wt%) was performed toward  $\text{Ni}_3\text{N}/\text{W}_5\text{N}_4$  hybrid structure. Interestingly, after removing the  $\text{Ni}_3\text{N}$  nanoparticles, a large number of pedestals shaped like a bowl can still be well retained at the corresponding position (Fig. 1e and Fig. S4), which implies that the Janus nanostructure is probably formed at the heterointerface between  $\text{Ni}_3\text{N}$  and  $\text{W}_5\text{N}_4$ .

To further reveal the detailed morphology and crystalline structure

of  $\text{Ni}_3\text{N}/\text{W}_5\text{N}_4$ , transmission electron microscopy (TEM) was conducted. As shown in Fig. 2a, the  $\text{Ni}_3\text{N}/\text{W}_5\text{N}_4$  is comprised of uniform nanoparticles and ultrathin nanosheets, and two components intertwined with each other. The high-resolution TEM (HRTEM) exhibits the lattice spacing of 0.51 nm and 0.243 nm, which can be well ascribed to the (002) and (101) planes of hexagonal  $\text{W}_5\text{N}_4$ , and the interplanar spacing of 0.218 nm and 0.188 nm belong to (002) and (102) planes of  $\text{Ni}_3\text{N}$  (Fig. 2b). Furthermore, the inset of Fig. 2b and other selected regions (Fig. S5) show clear heterointerface between hexagonal  $\text{W}_5\text{N}_4$  and  $\text{Ni}_3\text{N}$ . The selected area electron diffraction (SAED) pattern displays that the diffraction rings consist of discrete points, demonstrating the polycrystalline characters of  $\text{Ni}_3\text{N}/\text{W}_5\text{N}_4$ , and the diffraction spots can be assigned to (111) and (002) planes for  $\text{Ni}_3\text{N}$  and (002) planes for  $\text{W}_5\text{N}_4$  (Fig. 2c). The energy dispersive spectrometer (EDS) (Fig. 2d) shows the existence of N, Ni and W atoms, and the corresponding atom molar ratio is closed to 8:7:5, which also match well with the crystalline phase of  $\text{Ni}_3\text{N}$  and  $\text{W}_5\text{N}_4$ . Meanwhile, the EDS line scan were performed to investigate the in-depth morphology structure of  $\text{Ni}_3\text{N}/\text{W}_5\text{N}_4$  heterostructure. Interestingly, the W atoms appear on the outer layer, whereas the Ni atoms distribute in the inner layer, which indicates that the core of  $\text{Ni}_3\text{N}$  nanoparticles were likely to be wrapped via the  $\text{W}_5\text{N}_4$  shell. In addition, the high-angle annular dark-field scanning TEM (HAADF-STEM) and energy-dispersive X-ray spectroscopy (EDS) mapping results further reveal that the W and N atoms uniformly distributed on the surface of  $\text{Ni}_3\text{N}$  NPs (Fig. 2g and Fig. S6). To acquire more information about the core-shell structure, the TEM images of  $\text{W}_5\text{N}_4$  were also characterized. As shown in Fig. S7, after acidification process, the  $\text{Ni}_3\text{N}$  NPs were leached, and the bowl-like  $\text{W}_5\text{N}_4$  2D ultrathin nanosheets were obviously left at the relevant positions, which is consistent with the results from SEM. Based on the analysis above, the  $\text{Ni}_3\text{N}/\text{W}_5\text{N}_4$

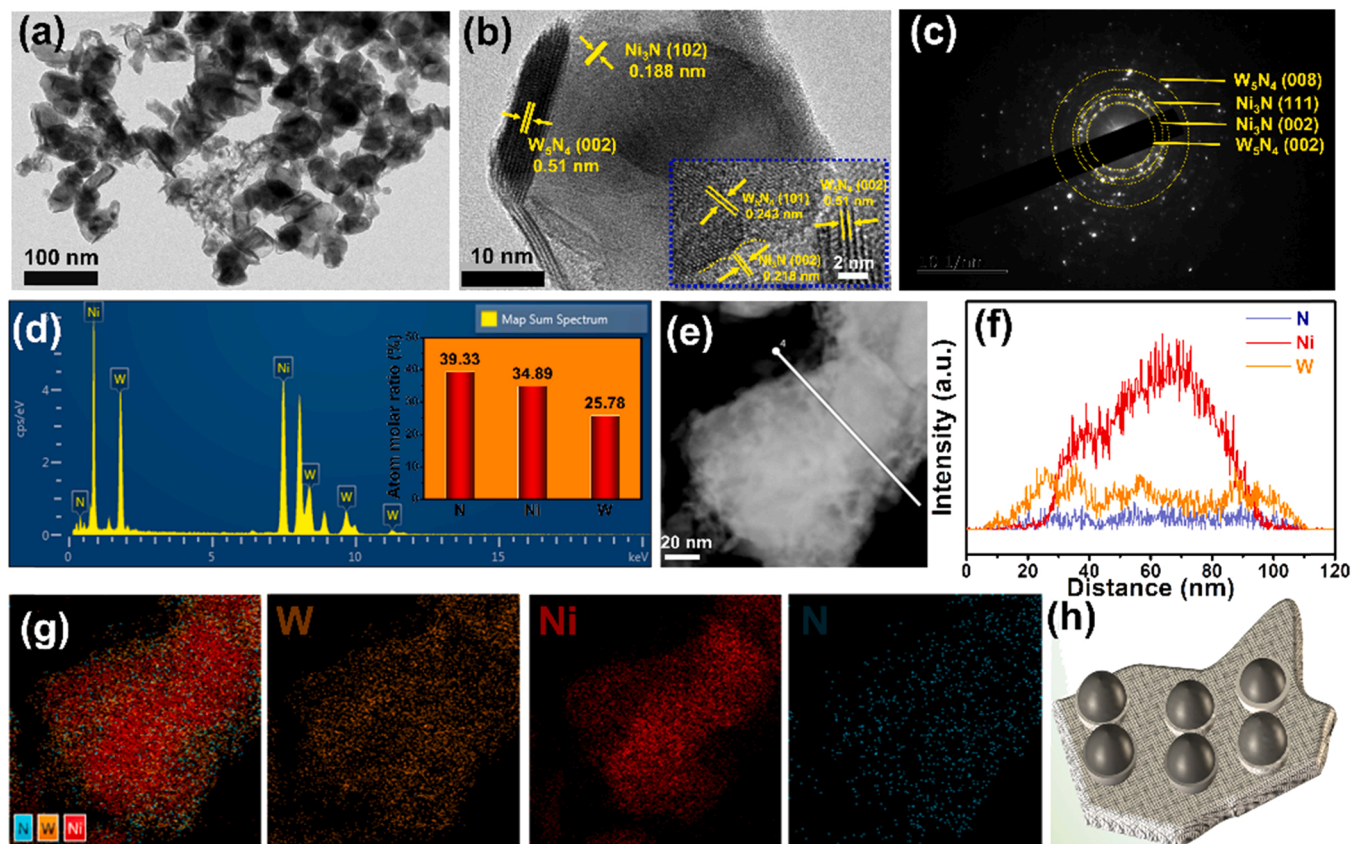


**Fig. 2.** (a) Low-resolution TEM image of catalysts peeled off from  $\text{Ni}_3\text{N}/\text{W}_5\text{N}_4$  heterostructures grown on Ni foam. (b) The HRTEM of  $\text{Ni}_3\text{N}/\text{W}_5\text{N}_4$  and the inset shows the interface between  $\text{Ni}_3\text{N}$  and  $\text{W}_5\text{N}_4$ . (c) The SAED pattern of this region. (d) The EDS spectra for  $\text{Ni}_3\text{N}/\text{W}_5\text{N}_4$  and the corresponding composition analysis from EDS results. (e-f) EDS line scan of  $\text{Ni}_3\text{N}/\text{W}_5\text{N}_4$  heterostructures. (g) High-resolution EDS elements maps of  $\text{Ni}_3\text{N}/\text{W}_5\text{N}_4$ . (h) The schematic diagram of 3D sponge-like  $\text{Ni}_3\text{N}/\text{W}_5\text{N}_4$  Janus structures.

heterostructure was comprised of a sponge-like network assembled from  $W_5N_4$  ultrathin nanosheets and  $Ni_3N$  nanoparticles, and the Janus nanostructure was formed at the interface between  $Ni_3N$  and  $W_5N_4$  (Fig. 2h). Typically, compared to conventional heterointerface (hierarchical interface and planar interface), Janus nanostructures will expose more densities of active interface and form the strong combination between two components, which is beneficial for the activity and stability of catalysts. The special Janus nanostructures of  $Ni_3N/W_5N_4$  motivate us to unveil the mechanism of its formation. Consequently, the calcination temperature-dependent experiments were carried out to investigate the evolution of crystalline phases and morphologies. As shown in Fig. S8, the phase transformation of  $NiW-OH$  precursors happened at 450 °C and the phase of  $Ni_3N$  began to form. Then, the hexagonal phase of  $W_5N_4$  appears at 500 °C along with the increased amount of  $Ni_3N$  phase. With the calcination temperature increasing, the  $NiW-OH$  precursors has been totally converted into  $Ni_3N/W_5N_4$  Janus nanostructure at 550 °C. Impressively, the continuous increased temperature will not lead to further growth and aggregation of  $Ni_3N$  NPs, demonstrating the significant nano-confinement effect of  $W_5N_4$  nanosheets (Fig. S9). It is noteworthy that, the presence of  $Ni_3N$  is essential for the formation of hexagonal  $W_5N_4$ . As demonstrated in Fig. S10, in the absence of  $Ni$  precursors, the ammonium tungsten partial will transform into cubic  $\beta$ -WN after nitridation process. Therefore, we proposed that the  $Ni_3N$  NPs formed at the earlier stage of nitridation process may act as a template of substrate and then the hexagonal  $W_5N_4$  nanosheets grown on the surface of  $Ni_3N$  NPs via domain matching epitaxy [19,38]. Meanwhile, the other transitional metal nitrides, such as  $Co_4N$  and  $Fe_4N$  can also induce the formation of  $W_5N_4$  nanosheets and generate the Janus nanostructures of  $Co_4N/W_5N_4$  and  $Fe_4N/W_5N_4$ , respectively (Fig. S11–15). In this regard, transition metal nitrides have a certain universality for inducing the generation of hexagonal  $W_5N_4$  nanosheets and forming the Janus heterostructure. Generally, the electronic structure of W atoms will be effectively tuned via N atoms, and hence the catalytical performance of  $W_xN$  will largely dependent on the ratio of N versus W atoms and the crystalline phase structure [39,40].

### 3.2. Electronic structure characterizations of $Ni_3N$ , $W_5N_4$ and $Ni_3N/W_5N_4$ Janus structure

The X-ray photoelectron spectroscopy (XPS) was used to get insights into the surface chemical composition and electronic interaction. The XPS survey spectra (Fig. 3a) clearly exhibits the coexistence of W, Ni and N atoms for  $Ni_3N/W_5N_4$  Janus structure. The Ni atoms disappear and only W and N atoms exist in  $W_5N_4$  nanosheets, further demonstrating that the  $Ni_3N$  NPs were almost totally removed after dealloying process. The high-resolution XPS spectrum of Ni 2p for  $Ni_3N/W_5N_4$  includes two main chemical states of Ni. In details, the deconvoluted peaks at 852.8 and 870.3 eV can be attributed to Ni-N bonds, and the peaks at 856.1 and 874 eV correspond to the Ni-O bond, which was inevitably aroused from oxidation in the air [41,42]. Besides, compared to  $Ni_3N/W_5N_4$ , the Ni 2p of pure  $Ni_3N$  NPs shows the similar XPS spectra and no distinct peak shift was observed, which indicates that the electronic interaction between  $Ni_3N$  and  $W_5N_4$  is negligible. In the W 4f spectra of  $Ni_3N/W_5N_4$ , the peaks at 32.1 and 34.2 eV belong to the bond of W-N, and the existence of W-O bond can also be identified via the peaks at 34.8 and 36.9 eV [43,44]. Similarly, the electron states of W in  $Ni_3N/W_5N_4$  also exhibits no changes compare to that of single phase of  $W_5N_4$ . Simultaneously, the N 1s spectra of  $Ni_3N/W_5N_4$  displays the peaks at 390.1, 397.9 and 399.4 eV, which can be ascribed to W-N, Ni-N and graphitic N, respectively and there still no electron accumulation and depletion occurs at the heterointerface between  $Ni_3N$  and  $W_5N_4$ . In order to acquire more insightful information about electron states on the surface, the work function of  $Ni_3N$ ,  $W_5N_4$  and  $Ni_3N/W_5N_4$  Janus nanostructure were investigated via the ultraviolet photoelectron spectroscopy (UPS). As shown in Fig. 3e, the  $Ni_3N$  and  $W_5N_4$  samples not only exhibit the metallic characters but also the approximate work function ( $\sim 4.79$  eV), which suggests that the electron transfer will not happen and hence the barrier-free Janus interface has formed between  $W_5N_4$  and  $Ni_3N$ . In contrast, due to the difference toward work function or Fermi level, conventional heterointerface will easily result in the electron redistribution and induce the Schottky barrier or built-in electric field at

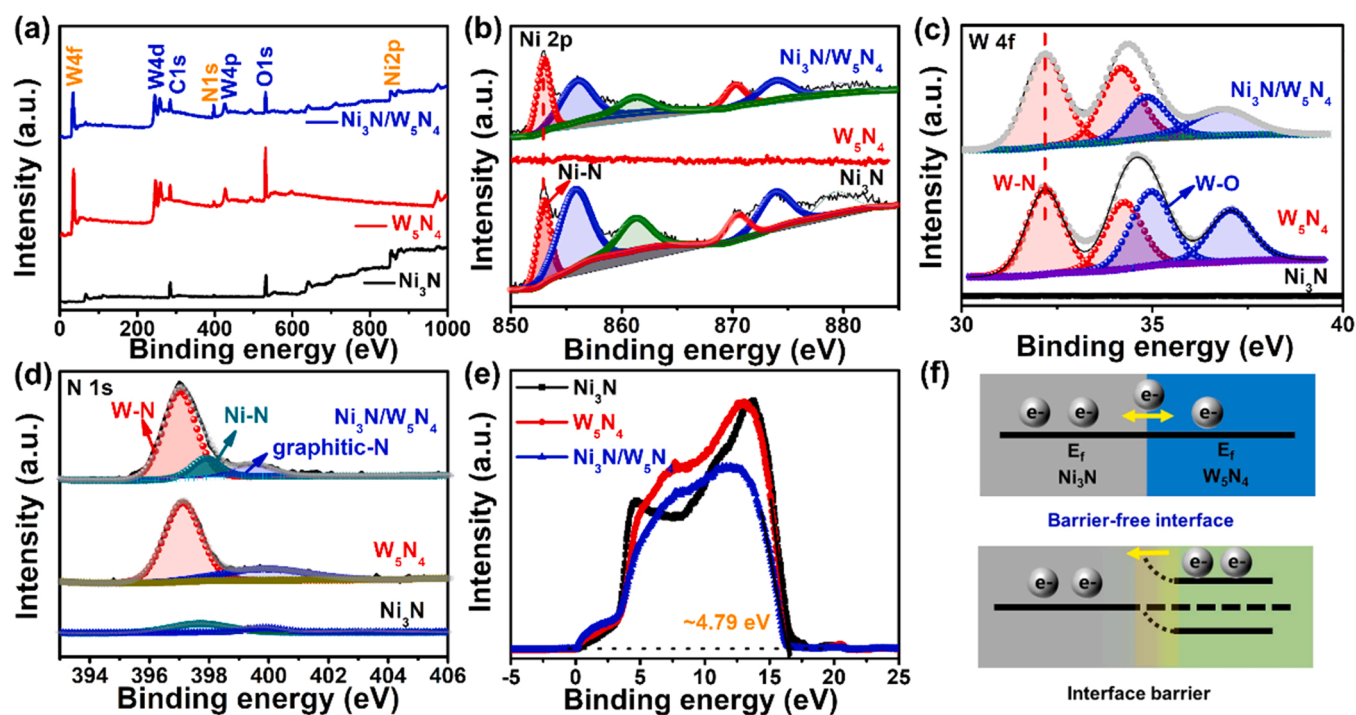
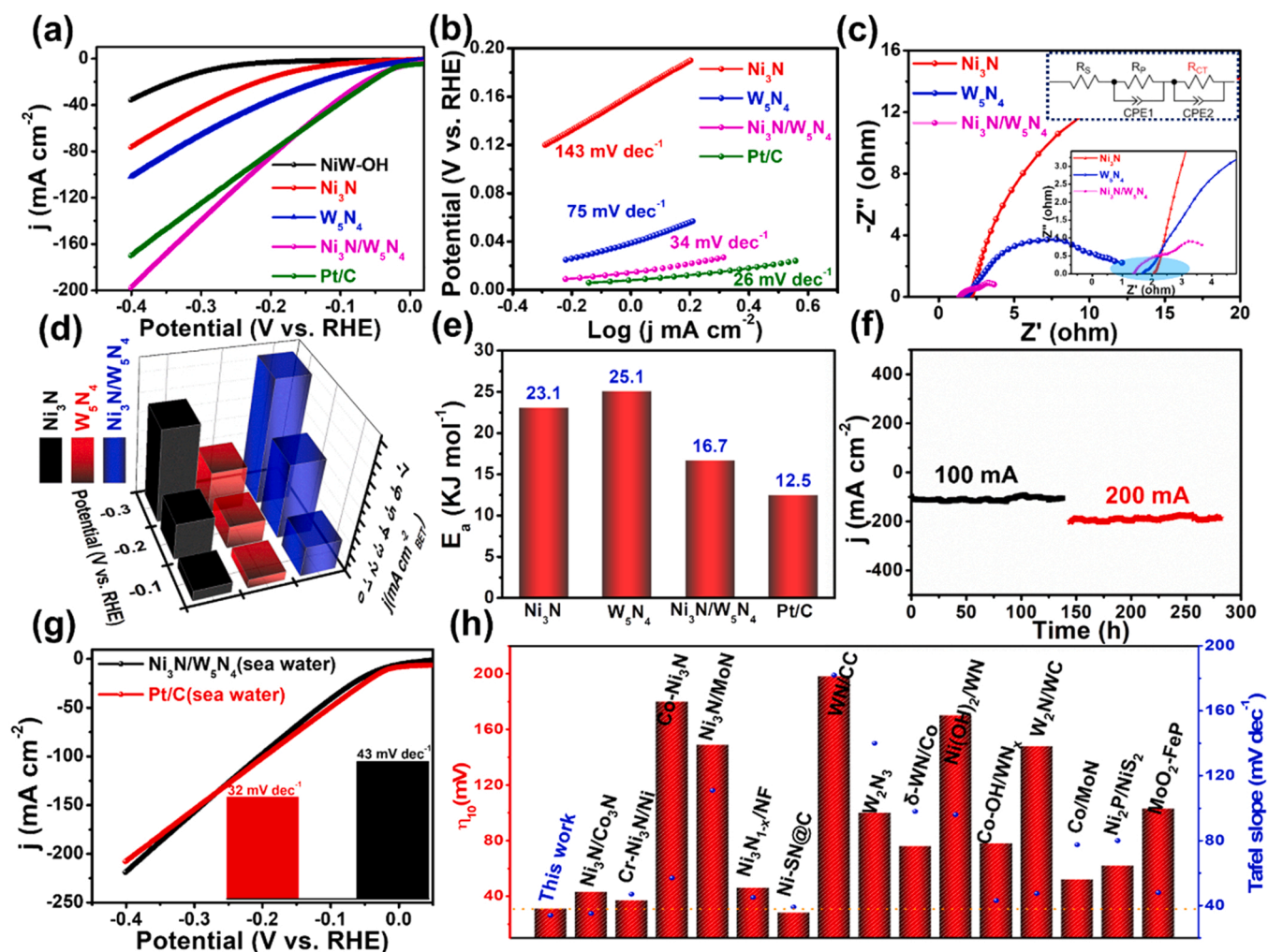


Fig. 3. (a) XPS survey spectra of  $Ni_3N$  NPs,  $W_5N_4$  nanosheets and  $Ni_3N/W_5N_4$  Janus structure. (b–d) High-resolution XPS spectra of Ni 2p, W 4f and N 1s for these samples, respectively. (e) UPS spectra of  $Ni_3N$ ,  $W_5N_4$  and  $Ni_3N/W_5N_4$ . (f) The comparison of schematic electron states at the interface for  $Ni_3N/W_5N_4$  and traditional Schottky interface.





**Fig. 4.** Electrochemical HER performance (without iR corrected). (a) The HER polarization curves in 1 M KOH and the corresponding Tafel plots (b) of NiW-OH, Ni<sub>3</sub>N, W<sub>5</sub>N<sub>4</sub> and Ni<sub>3</sub>N/W<sub>5</sub>N<sub>4</sub> Janus structure. (c) Nyquist plots of different catalysts measured at -0.95 V, and the inset represent the equivalent circuit. (d) The current density calculated by normalizing to the specific surface area at the overpotential of -0.1, -0.2 and -0.3 V. (e) The activation energy of Ni<sub>3</sub>N, W<sub>5</sub>N<sub>4</sub>, Ni<sub>3</sub>N/W<sub>5</sub>N<sub>4</sub> and commercial Pt/C at the zero overpotential. (f) The long-term stability for Ni<sub>3</sub>N/W<sub>5</sub>N<sub>4</sub> operated at the overpotential -0.2 and -0.4 V, respectively. (g) The LSV polarization curves in alkaline seawater for Ni<sub>3</sub>N/W<sub>5</sub>N<sub>4</sub> and Pt/C, and the inset represents the corresponding Tafel slope. (h) Comparison of overpotential and Tafel slope for Ni<sub>3</sub>N/W<sub>5</sub>N<sub>4</sub> Janus structure and previously reported Ni, W-based and other non-noble metal catalysts.

heterointerface. However, the unidirectional rectification characteristics of Schottky interface or p-n junction will not benefit for the design of bifunctional catalysts [28]. In this respect, the Ni<sub>3</sub>N/W<sub>5</sub>N<sub>4</sub> hybrid structure, with distinguished 3D sponge-like Janus structure and barrier-free heterointerface, is expected to be a promising bifunctional electrocatalyst.

### 3.3. Hydrogen evolution reaction measurement

The electrochemical hydrogen evolution reaction (HER) activities were evaluated in 1 M KOH electrolyte with a typical three-electrode system (without iR compensation). As shown in Fig. 4a, the Ni<sub>3</sub>N/W<sub>5</sub>N<sub>4</sub> electrode exhibits apparently lower overpotential and higher current density than that of pure Ni<sub>3</sub>N and W<sub>5</sub>N<sub>4</sub>, indicating that the designed Janus interfaces are essential for the enhanced HER performance. Impressively, the Ni<sub>3</sub>N/W<sub>5</sub>N<sub>4</sub> Janus nanostructure displays Pt-like HER performance with an ultralow overpotential of 31 mV at 10 mA, which is much lower than that of NiW-OH (289 mV), Ni<sub>3</sub>N (166 mV) and W<sub>5</sub>N<sub>4</sub> (80 mV), and outperforms various kinds of previously reported Ni and W based heterostructure catalysts (Fig. 4h, Table S1). To explore the catalytic kinetics mechanism of the synthesized electrodes, Tafel plots derived from the polarization curves are

calculated in Fig. 4b. The Tafel slope for Ni<sub>3</sub>N/W<sub>5</sub>N<sub>4</sub> hybrid electrode is about 34 mV dec<sup>-1</sup>, which suggests that the Volmer-Heyrovsky mechanism is the main reaction routine, and the Heyrovsky step is viewed as the rate-determining step. In contrast, for Ni<sub>3</sub>N electrode, the Tafel slope is 143 mV dec<sup>-1</sup>, illustrating the sluggish water dissociation process. Meanwhile, the W<sub>5</sub>N<sub>4</sub> with Tafel slope of 75 mV dec<sup>-1</sup> shows much better water dissociation capability than Ni<sub>3</sub>N, but the overall HER kinetics still inferior to Ni<sub>3</sub>N/W<sub>5</sub>N<sub>4</sub>. Together, these results demonstrate the remarkable improved reaction kinetics for Ni<sub>3</sub>N/W<sub>5</sub>N<sub>4</sub> than that of Ni<sub>3</sub>N and W<sub>5</sub>N<sub>4</sub>, which could be ascribed to the synergetic effect of Janus interface. The electrochemical impedance spectroscopy (EIS) was also characterized to further study the electrochemical kinetics. As is shown in Fig. 4c, the equivalent circuit was provided, which illustrates that the Ni<sub>3</sub>N/W<sub>5</sub>N<sub>4</sub> heterostructure possess the lower interface charge transfer resistance and superior electron transfer capability than that of Ni<sub>3</sub>N and W<sub>5</sub>N<sub>4</sub>, further suggesting the more favorable kinetics for Ni<sub>3</sub>N/W<sub>5</sub>N<sub>4</sub>.

Generally speaking, the electrochemical performance will largely depend on the number of active sites and the intrinsic catalytic activity. As shown in Fig. S16, the Brunauer-Emmett-Teller (BET) measurement of W<sub>5</sub>N<sub>4</sub> nanosheets exhibit the largest surface area of 28.9 g cm<sup>-3</sup>, larger than that of Ni<sub>3</sub>N (8.3 g cm<sup>-3</sup>) and Ni<sub>3</sub>N/W<sub>5</sub>N<sub>4</sub> (20.8 g cm<sup>-3</sup>), which is likely ascribed to the more exposed ultra-thin nanosheets after

removing Ni<sub>3</sub>N NPs. Unexpectedly, the electrochemically active surface areas (ECSA) are 234 mF cm<sup>-2</sup>, 96 mF cm<sup>-2</sup> and 12 mF cm<sup>-2</sup> for the Ni<sub>3</sub>N/W<sub>5</sub>N<sub>4</sub>, W<sub>5</sub>N<sub>4</sub> and Ni<sub>3</sub>N, respectively, indicating the large number of active sites for Ni<sub>3</sub>N/W<sub>5</sub>N<sub>4</sub> [45]. Meanwhile, the direct comparison of intrinsic activities for Ni<sub>3</sub>N, W<sub>5</sub>N<sub>4</sub> and Ni<sub>3</sub>N/W<sub>5</sub>N<sub>4</sub> were normalized via specific surface area calculated from BET. Fig. S17 and Fig. 4d depict that, compared to single component of Ni<sub>3</sub>N and W<sub>5</sub>N<sub>4</sub>, the Ni<sub>3</sub>N/W<sub>5</sub>N<sub>4</sub> Janus structure illustrates more excellent intrinsic catalytic performance at a wide potential range (−0.4 to 0 V). Especially, at the overpotential of −200 mV, the intrinsic performance of Ni<sub>3</sub>N/W<sub>5</sub>N<sub>4</sub> is two and three-fold times better than Ni<sub>3</sub>N and W<sub>5</sub>N<sub>4</sub>, respectively. Moreover, the activation energy (*E*<sub>a</sub>) of HER is another important feature to evaluate the intrinsic activities of electrodes, which only depends on material composition but not the surface area and other extrinsic factors [46,47]. As exhibited in Fig. 4e and Fig. S18, the *E*<sub>a</sub> at the zero overpotential for Ni<sub>3</sub>N/W<sub>5</sub>N<sub>4</sub> Janus structure is 16.7 kJ mol<sup>-1</sup>, comparable to that of Pt/C

(12.5 kJ mol<sup>-1</sup>) and much better than that of Ni<sub>3</sub>N (23.1 kJ mol<sup>-1</sup>) and W<sub>5</sub>N<sub>4</sub> (25.1 kJ mol<sup>-1</sup>), further confirming the remarkable intrinsic activity for this Janus nanomaterial.

Importantly, except for the outstanding HER activity, the Ni<sub>3</sub>N/W<sub>5</sub>N<sub>4</sub> Janus structure also exhibits the excellent stability. As displayed in Fig. 4f, the chronoamperometric curve recorded at constant voltage of −0.2 V and −0.4 V were performed, and the industrially relevant current of 100 and 200 mA was retained with negligible attenuation for ~300 h, indicating the extremely high durability for Ni<sub>3</sub>N/W<sub>5</sub>N<sub>4</sub> hybrid materials. Meanwhile, the Faradic efficiency of generating hydrogen production is close to 100% during this process (Fig. S19). To further estimate the practical application capability, the HER performance of Ni<sub>3</sub>N/W<sub>5</sub>N<sub>4</sub> electrode were also measured in alkaline seawater (Fig. S20). Fig. 4g and Fig. S21 show that the Ni<sub>3</sub>N/W<sub>5</sub>N<sub>4</sub> also exhibits excellent HER performance (36 mV at 10 mA) and favorable HER kinetics (43 mV dec<sup>-1</sup>), which is comparable to commercial Pt/C and much

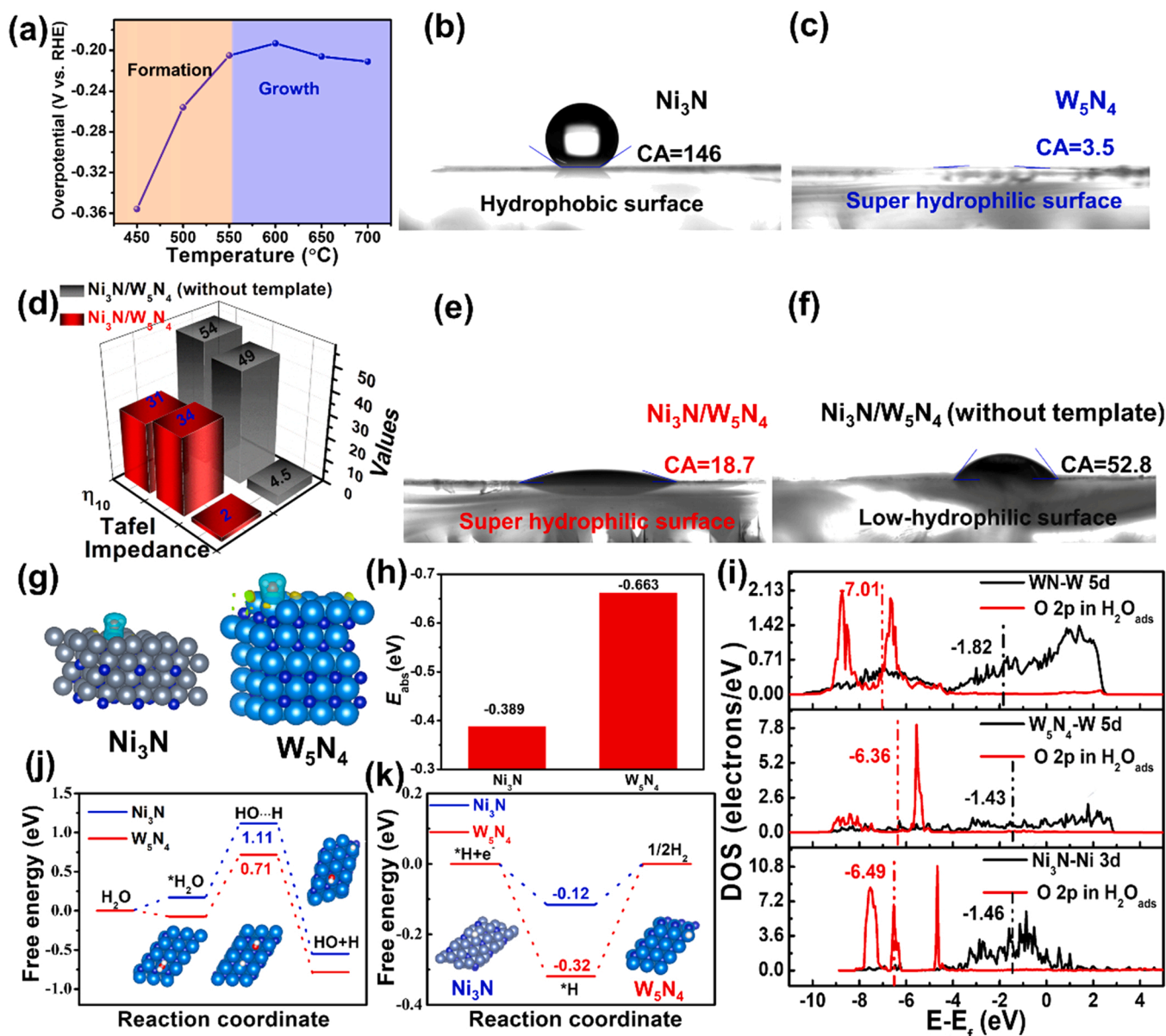


Fig. 5. (a) The required overpotentials to drive 100 mA of these catalysts prepared at different temperature. (b) Water contact-angle characterizations of Ni<sub>3</sub>N and (c) W<sub>5</sub>N<sub>4</sub>. (d) Comparisons toward  $\eta_{10}$ , Tafel slope and impedance between Ni<sub>3</sub>N/W<sub>5</sub>N<sub>4</sub> and Ni<sub>3</sub>N/W<sub>5</sub>N<sub>4</sub> (without template). (e) Water contact-angle characterizations of Ni<sub>3</sub>N/W<sub>5</sub>N<sub>4</sub> and (f) Ni<sub>3</sub>N/W<sub>5</sub>N<sub>4</sub> (without template). (g) The difference charge density of Ni<sub>3</sub>N and W<sub>5</sub>N<sub>4</sub> with adsorbed water molecules. (h) The water adsorption energies of Ni<sub>3</sub>N and W<sub>5</sub>N<sub>4</sub>. (i) The PDOS plots of Ni 3d in Ni<sub>3</sub>N and W 5d in W<sub>5</sub>N<sub>4</sub> and WN after H<sub>2</sub>O adsorption (black line), and O 2p in H<sub>2</sub>O on the corresponding three surfaces, respectively. (j) The calculated relative energy diagrams for H<sub>2</sub>O dissociation and (k) H adsorption on Ni<sub>3</sub>N and W<sub>5</sub>N<sub>4</sub>.



better than  $\text{Ni}_3\text{N}$  and  $\text{W}_5\text{N}_4$ . More importantly, the  $\text{Ni}_3\text{N}/\text{W}_5\text{N}_4$  electrode still possesses the outstanding durability under the large current (100 mA), indicating the superior capability for corrosion-resistant from chloride environment. Furthermore, the XRD, XPS and SEM for  $\text{Ni}_3\text{N}/\text{W}_5\text{N}_4$  Janus nanostructure were collected after the durability measurement (Fig. S22–24). Both the crystal structure and morphology are well maintained after HER process, further demonstrating the robustness of  $\text{Ni}_3\text{N}/\text{W}_5\text{N}_4$  Janus structure.

### 3.4. The structure-activity relationships and catalysis mechanism

Moreover, comprehensive experiments and DFT calculations were performed to investigate the reasons why  $\text{Ni}_3\text{N}/\text{W}_5\text{N}_4$  Janus nanostructure possesses Pt-like HER performance. During the formation process of  $\text{Ni}_3\text{N}/\text{W}_5\text{N}_4$  Janus structure (450–550 °C), the activity ( $\eta_{100}$ ) is gradually improved, which disclose the critical role of heterointerface between  $\text{Ni}_3\text{N}$  and  $\text{W}_5\text{N}_4$  (Fig. 5a and Fig. S25). At the growth region (550–700 °C), the  $\text{Ni}_3\text{N}/\text{W}_5\text{N}_4$  electrode prepared at 600 °C exhibits the most superior activity. Then, with the increased temperature, almost no variations of HER performance occur for these electrodes. To understand the synergistic effect between  $\text{Ni}_3\text{N}$  and  $\text{W}_5\text{N}_4$  heterointerface, the contact-angle measurements were carried out for  $\text{Ni}_3\text{N}$  NPs and  $\text{W}_5\text{N}_4$  2D nanosheets, respectively. Impressively,  $\text{Ni}_3\text{N}$  NPs are distinctly different from  $\text{W}_5\text{N}_4$  in terms of wettability. The contact-angle between  $\text{Ni}_3\text{N}$  and water was characterized to be 146° (Fig. 5b), suggesting the hydrophobic surface of  $\text{Ni}_3\text{N}$ . In contrast,  $\text{W}_5\text{N}_4$  nanosheets exhibit the super hydrophilic character, showing the contact-angle of 3.5°. These results indicates that  $\text{W}_5\text{N}_4$  is likely to act as a water pump, that could effectively adsorb and dissociate the  $\text{H}_2\text{O}$  into  $\text{H}^*$  and  $\text{OH}^-$ , and  $\text{Ni}_3\text{N}$  is probably considered as the sites of  $\text{H}^*$  adsorption and subsequent formation of  $\text{H}_2$ . In addition, compared to the hexagonal phase of  $\text{W}_5\text{N}_4$  (Fig. S26), the cubic phase of WN displays the terrible HER performance and the sluggish Volmer process (water dissociation), suggesting the advantages of  $\text{W}_5\text{N}_4$  components. Except for the advantages of components, the merits of multilevel sponge-like Janus structure were also analyzed. For the sake of comparison, the sample, denoted as “ $\text{Ni}_3\text{N}/\text{W}_5\text{N}_4$  without template” was synthesized without the template of  $\text{Ni}(\text{OH})_2$  nanosheets (Fig. S27 and 28). As shown in Fig. 5d and Fig. S29, the 3D sponge-like  $\text{Ni}_3\text{N}/\text{W}_5\text{N}_4$  Janus nanostructure exhibits the lower overpotential and faster kinetics than that of  $\text{Ni}_3\text{N}/\text{W}_5\text{N}_4$  heterostructure (without template). Moreover, the contact-angle measurements of these two samples were also characterized (Figs. 5e and 5f). The  $\text{Ni}_3\text{N}/\text{W}_5\text{N}_4$  Janus structure possess the super hydrophilic surface ( $\text{CA}=18.7^\circ$ ), which inherit the hydrophilic character of  $\text{W}_5\text{N}_4$ . However, the  $\text{Ni}_3\text{N}/\text{W}_5\text{N}_4$  (without template) shows the low-hydrophilic surface with the CA of 52.8°, further demonstrating the advantage of 3D sponge-like Janus structure of  $\text{Ni}_3\text{N}/\text{W}_5\text{N}_4$ . Besides, the samples of  $\text{Ni}_3\text{N}/\text{W}_5\text{N}_4$  Janus structure with different Ni/W atomic ratio were also investigated, and  $\text{Ni}_3\text{N}/\text{W}_5\text{N}_4$  (Ni:W~1:1) electrode studied in our work shows the superior HER activity (Fig. S30).

To unveil the synergistic effect of  $\text{Ni}_3\text{N}/\text{W}_5\text{N}_4$  Janus interface at the atomic levels, the density functional theory (DFT) calculations were performed. In consideration of the fact that the water adsorption, dissociation and the subsequent adsorption/desorption of  $\text{H}^*$  are critical for HER in alkaline solutions, we comprehensively investigated these behaviors on the  $\text{Ni}_3\text{N}$  and  $\text{W}_5\text{N}_4$  surface. The difference charge density between  $\text{W}_5\text{N}_4$  and adsorbed  $\text{H}_2\text{O}$  molecular exhibits the more apparent electron accumulation and deletion than that of  $\text{Ni}_3\text{N}$  (Fig. 5g), indicating the stronger interaction. The calculated  $\text{H}_2\text{O}$  adsorption energies of  $\text{W}_5\text{N}_4$  (−0.663 eV) and  $\text{Ni}_3\text{N}$  (−0.389 eV) further illustrate that the water adsorption on W atoms in  $\text{W}_5\text{N}_4$  is much stronger than that on Ni atoms in  $\text{Ni}_3\text{N}$  (Fig. 5h). Typically, the higher d orbital energies of catalysts and lower p orbitals energies of adsorbed  $\text{H}_2\text{O}$  molecule are unfavorable for the interfacial charge interaction and thus affect the subsequent water adsorption and dissociation process [48]. Based on this point, the d orbital electronic structure of  $\text{Ni}_3\text{N}$ ,  $\text{W}_5\text{N}_4$ , WN as well as

p orbital local density of states analysis of oxygen atom for adsorbed water were systematically studied [49]. Fig. 5i clearly exhibits that the active W 4d and O 2p have the largest electronic overlap (the energy gap) on the  $\text{W}_5\text{N}_4$ , demonstrating the superior water adsorption capability. Especially, the electronic overlap between W 4d and O 2p on WN (−8.84 eV) is much lower than that of  $\text{W}_5\text{N}_4$  (−7.79 eV), which is consistent with the experiment results and further reflect the advantages of composition toward the activation of  $\text{H}_2\text{O}$  molecule. Besides, the electron density near the Fermi level of  $\text{W}_5\text{N}_4$  is higher than that of WN, suggesting the excellent electron transport capability of  $\text{W}_5\text{N}_4$  (Fig. S31). Meanwhile, the relative energy profile (Fig. 5j) of water dissociation further reveals that  $\text{W}_5\text{N}_4$  exhibits a much lower energy barrier (0.71 eV) than  $\text{Ni}_3\text{N}$  (1.11 eV), which means that  $\text{W}_5\text{N}_4$  will offer the favorable sites for water adsorption and activation process. In addition, the adsorption free energy of hydrogen ( $\Delta G_{\text{H}}$ ) is another important criterion for the subsequent  $\text{H}_2$  generation process, and the catalysts with near zero hydrogen adsorption energy ( $\Delta G_{\text{H}}=0$ ) are considered to be the promising candidate for HER. Interestingly, the relative free energy diagram of  $\text{H}^*$  exhibits that (Fig. 5k), compared to that of  $\text{W}_5\text{N}_4$  (−0.32 eV), the  $\text{Ni}_3\text{N}$  shows the preferable  $\text{H}^*$  adsorption kinetics with an energy of −0.12 eV. The favorable  $\text{H}^*$  adsorption indicates that the  $\text{Ni}_3\text{N}$  NPs could provide appropriate sites for the combination of  $\text{H}^*$  and then realize the whole HER process. To sum up, the unique Janus heterointerface system endows  $\text{Ni}_3\text{N}/\text{W}_5\text{N}_4$  with excellent HER activity via the interface synergistic effects and advantages of 3D sponge-like structure.

### 3.5. The performance of plastics upgrading

Furthermore, considering the serious pollution of PET (a common plastic), the upcycling of PET via electrochemical oxidation was attempted on  $\text{Ni}_3\text{N}/\text{W}_5\text{N}_4$  electrode. Strikingly, the upgrading of plastics exhibits the remarkably improved activity compared to the sluggish OER process. As is shown in Fig. 6a, only 1.33 V was required to drive the current density of 10  $\text{mA cm}^{-2}$  for PET oxidation, which is much lower than that of 1.54 V for OER, which suggests that the PET upcycling is more energy-saving than OER. Moreover, the current density of PET oxidation at different potentials (1.5, 1.55, 1.6 and 1.65 V) was over 3–5 times larger than corresponding OER, implies that PET reforming will also in return boost the hydrogen generation on the counter electrode (Fig. 6b). Furthermore, the effect of PET concentration toward plastics upgrading activity of  $\text{Ni}_3\text{N}/\text{W}_5\text{N}_4$  electrode was also investigated. As shown in Fig. S32, the activity of PET upgrading will gradually increase with the increase of PET concentration. Finally, when the amount of PET exceed the weight of 2 g, the PET reforming performance become almost unchanged. To explore the production of PET reforming, the chronoamperometry was applied at different potentials (1.4, 1.45, 1.5, 1.55 and 1.6 V) for 1 h, and then the liquid products were analyzed via nuclear magnetic resonance (NMR) spectra (Fig. S33). As displayed in Fig. 6c and Fig. 6d,  $\text{HCOOH}$ , one of the important value-added chemicals, was selectively produced during the PET upgrading process and its production rate gradually increases with the increasing voltage. Meanwhile, the Faradic efficiency of generating  $\text{HCOOH}$  for  $\text{Ni}_3\text{N}/\text{W}_5\text{N}_4$  Janus structures was as high as ~85% at the potential range of 1.4–1.6 V, demonstrating the superior selectivity toward  $\text{HCOOH}$  production. Especially, under the large current density of 120  $\text{mA cm}^{-2}$  (operated at 1.6 V), the high  $\text{HCOOH}$  production rate of 1.2  $\text{mmol/h/cm}^2$  is achieved. It was noteworthy that, compared to conventional mechanical, chemical recycling as well as recent reported plastics reforming via photocatalysis, the electrochemical PET upgrading realizes the highly efficient activity and selectivity of value-added chemical products. Then, the durability for PET reforming was investigated via applying a constant potential of 1.6 V for 2 h, and a fresh alkaline solution with PET lysate was provided after each cycle. Fig. 6e and Fig. S34 show that the passing charge has negligible changes and the production of  $\text{HCOOH}$  maintains about ~2.2  $\text{mmol}$  after each cycle,

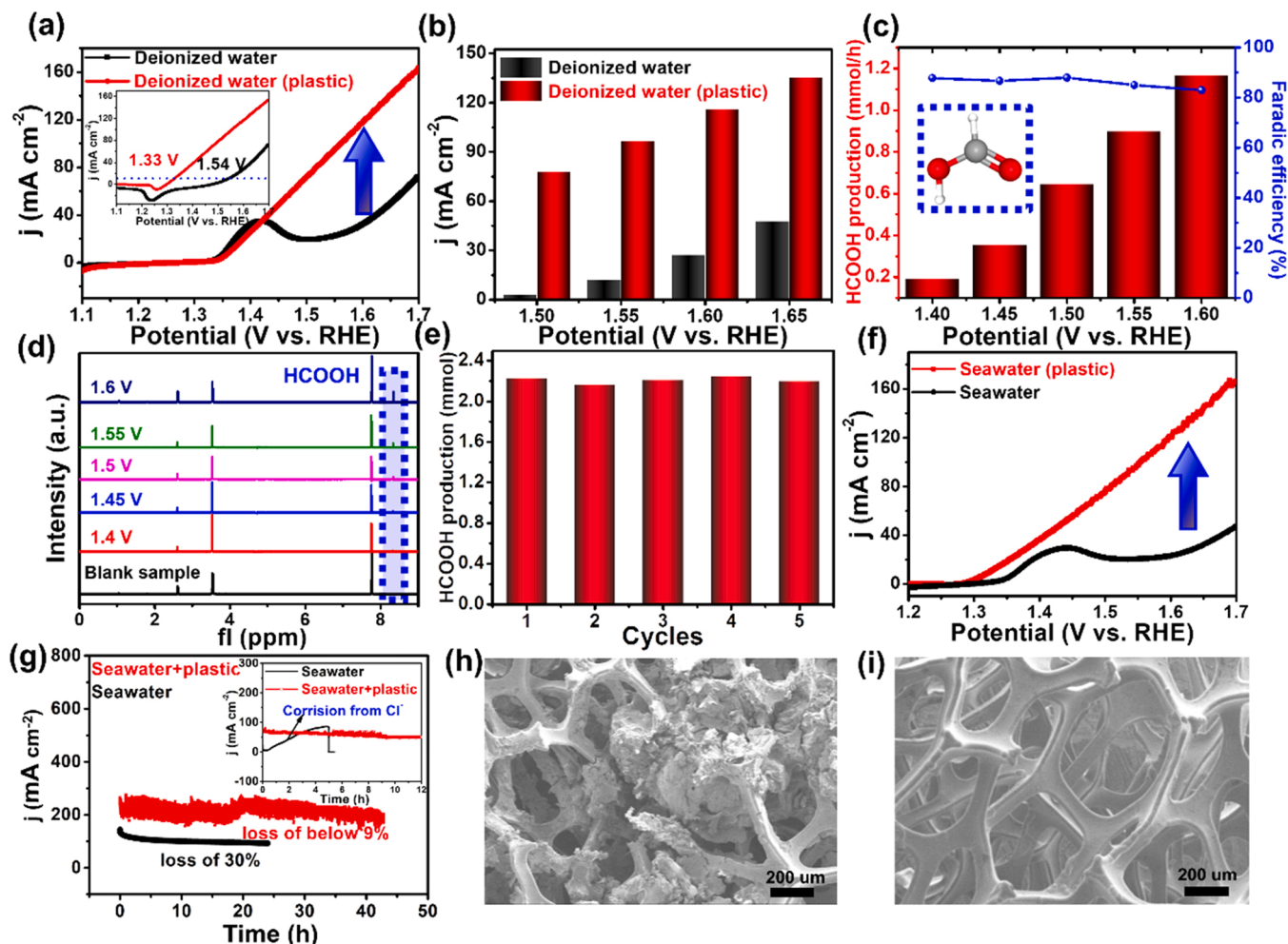


**Fig. 6.** Electrochemical PET upgrading performance (all results obtained without iR corrected). (a) LSV curves of  $\text{Ni}_3\text{N}/\text{W}_5\text{N}_4$  Janus structure with and without plastic in deionized water. (b) The corresponding current density under different potentials. (c) The HCOOH production rate and Faradic efficiency under different potentials. (d) <sup>1</sup>H NMR spectrums of solutions obtained after PET upgrading for 1 h under the potential of 1.4 V, 1.45 V, 1.5 V, 1.55 V and 1.6 V, respectively. (e) The relevant HCOOH production obtained after each cycle. (f) LSV curves of  $\text{Ni}_3\text{N}/\text{W}_5\text{N}_4$  Janus structure with and without plastic in seawater. (g) The durability test operated at 1.8 V in seawater (with and without PET) for  $\text{Ni}_3\text{N}/\text{W}_5\text{N}_4$  and Ni foam electrode (inset), respectively. (h) The relevant SEM after reaction of Ni foam with the absence and (i) presence of microplastic.

which suggesting the excellent stability of  $\text{Ni}_3\text{N}/\text{W}_5\text{N}_4$  Janus nanostructure toward PET upgrading.

Actually, plastic pollution in the ocean has become a common phenomenon, which seriously threatens the ecological security. In this regard, the PET upgrading for  $\text{Ni}_3\text{N}/\text{W}_5\text{N}_4$  was also carried out in the alkaline seawater. As illustrated in Fig. 6 f, similar to PET reforming in deionized water, the  $\text{Ni}_3\text{N}/\text{W}_5\text{N}_4$  Janus structure also achieves an ultralow  $\eta_{10}$  of 1.32 V during PET reforming process in seawater. Furthermore, compare to seawater splitting (without plastics), the significant enhanced current density occurs in the presence of plastics under the same driving potential. These results suggest that the energy-saving PET upgrading can still be proceed in real seawater. It is generally accepted that the bottleneck for seawater splitting is the chlorine evolution reaction (CER), and the electrode will be severely destroyed when the applied potential exceeds the safe voltage window between OER and CER (within  $\sim 1.72$  V vs. RHE). To our surprised, the PET reforming process will largely break the limited potential and enhance the safe voltage window. As exhibited in Fig. 6 g, under the potential of 1.8 V in alkaline seawater (without plastic lysate), the competing CER will happen and the  $\text{Ni}_3\text{N}/\text{W}_5\text{N}_4$  electrode starts to be corrode, which induce the decay of the anodic current density (loss of 30% for 24 h). In contrast, owing to the favorable PET reforming process, the CER process will significantly be inhibited with the presence of plastic lysate in

seawater. The  $\text{Ni}_3\text{N}/\text{W}_5\text{N}_4$  electrode remains excellent durability under the industrially relevant current ( $\sim 200$  mA) at the operating potential of 1.8 V (loss of below 9% for 45 h). Furthermore, the bare Ni foam electrode further remarkably confirms the extended safe operating voltage window. The inset in Fig. 6 g illustrates that the Ni foam will go through corrosion from Cl<sup>-</sup> and subsequently result in the electrode breakage in pure seawater. However, the Ni foam electrode is stable under the same condition, except for the existence of PET. The SEM images of Ni electrode after anodic reaction (with and without PET) reveal that the more serious corrosion (Fig. 6 h) occurs for seawater electrolysis than that of PET upgrading, in accordance with the aforementioned results. The increased safe voltage window is critical for industrial-scale hydrogen production and plastic degradation from seawater.

In addition, the LSV curves of  $\text{Ni}_3\text{N}$  and  $\text{W}_5\text{N}_4$  were also measured to study the origin of excellent PET upcycling performance for  $\text{Ni}_3\text{N}/\text{W}_5\text{N}_4$  Janus electrode. Fig. S35 displays that both  $\text{Ni}_3\text{N}$  and  $\text{W}_5\text{N}_4$  show a certain PET reforming activity, but still inferior to  $\text{Ni}_3\text{N}/\text{W}_5\text{N}_4$  electrode. The  $E_a$  values of  $\text{Ni}_3\text{N}$ ,  $\text{W}_5\text{N}_4$  and  $\text{Ni}_3\text{N}/\text{W}_5\text{N}_4$  were calculated to be 15.3, 15, 14.5 KJ mol<sup>-1</sup>, respectively. These results indicate that the excellent PET upcycling performance is attributed to the synergistic effect between  $\text{Ni}_3\text{N}$  and  $\text{W}_5\text{N}_4$ . After stability test, the SEM and TEM images of  $\text{Ni}_3\text{N}/\text{W}_5\text{N}_4$  were also characterized. Fig. S36 depicts that  $\text{Ni}_3\text{N}/\text{W}_5\text{N}_4$  electrode still maintained the 3D sponge-like structure but new

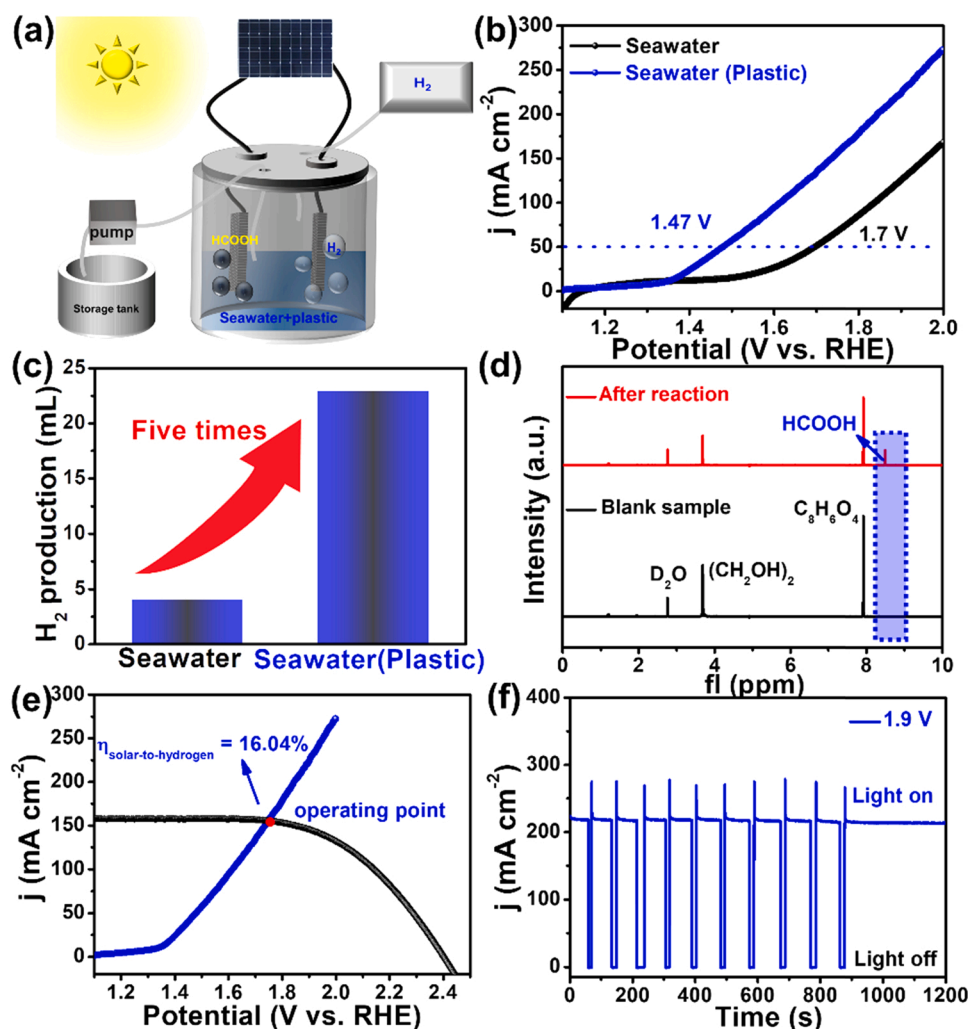


Fig. 7. (a) Schematic illustration of a small factory powered by solar energy for HER and plastics upgrading. (b) LSV curves of bifunctional Ni<sub>3</sub>N/W<sub>5</sub>N<sub>4</sub> catalyst performed in seawater (with and without plastics). (c) The amount of H<sub>2</sub> production and (e) <sup>1</sup>H NMR spectra collected after operating at 1.47 V for 2 h. (e) J-V characteristic curve of the commercial Si solar cell (under dark and light irradiation) and the corresponding  $\eta_{\text{solar-to-hydrogen}}$ . (f) The variation of photocurrent density under the absence and presence of sun (1.9 V).

nanosheets has formed on the Ni<sub>3</sub>N nanoparticles, and the W<sub>5</sub>N<sub>4</sub> nanosheets seems to be more roughness, which possibly results from its inevitable reconstruction during the oxidation process. The XRD pattern of Ni<sub>3</sub>N/W<sub>5</sub>N<sub>4</sub> only shows the character of Ni<sub>3</sub>N, and the W<sub>5</sub>N<sub>4</sub> phase has become low crystalline (Fig. S37). The XPS spectra (Fig. S38) reveal the presence of Ni<sup>2+</sup> and W<sup>6+</sup>, which indicates that the MOOH may be the real active sites for the C-C bond cleavage process, and hence enables the transformation from plastics to HCOOH [50]. The proposed reaction pathway toward electro-reforming of plastics were illustrated in Fig. S39. Firstly, the dehydrogenation process was happened on the OH and C-H group and formed the glyoxal. Then, the cleavage of C-C bond induce the formation of HCOOH.

### 3.6. Solar-driven HER coupled with plastics reforming based on Ni<sub>3</sub>N/W<sub>5</sub>N<sub>4</sub> Janus electrode

In view of the above exciting results, it is expected that the Ni<sub>3</sub>N/W<sub>5</sub>N<sub>4</sub> Janus structure could effectively drive both HER and plastic reforming process synchronously. Consequently, a small solar-driven “chemical factory” based on two electrode systems comprised of Ni<sub>3</sub>N/W<sub>5</sub>N<sub>4</sub> as both the cathode and anode were designed to directly catalyze HER and plastic upgrading from seawater (Fig. 7a and Fig. S40). For comparison, the seawater splitting electrolyzer (without plastics) was also investigated. As shown in Fig. 7b, the LSV curve of Ni<sub>3</sub>N/W<sub>5</sub>N<sub>4</sub> Janus structure exhibits the high voltages of 1.53 V and 1.7 V at the current density of 10 and 50 mA cm<sup>-2</sup> for seawater splitting,

respectively. However, with the presence of plastics, the required potentials to drive the current density of 10 and 50 mA cm<sup>-2</sup> were significantly decreased to 1.4 V and 1.47 V, respectively, which exceed the most reported bifunctional catalysts. Additionally, under the same potential of 1.47 V, the H<sub>2</sub> amount produced at seawater (with plastics) is about five times larger than that generated in pure seawater, indicating that plastic upgrading is a powerful pathway for energy-saving hydrogen production (Fig. 7c). Meanwhile, the HCOOH is effectively produced via plastic upgrading at the anode electrode with the Faradic efficiency of ~85% (Fig. 7d). Impressively, the integrated device exhibited a high current density of 156 mA cm<sup>-2</sup>, equivalent to a solar-to-hydrogen efficiency (STH) conversion efficiency of 16.04% under 1 sun illumination (Fig. 7e and Fig. S41), which is higher than most of the previous STH values to date (Table S2). Furthermore, the solar-driven chemical factory could stably operate under the industrially relevant current density of ~210 mA cm<sup>-2</sup> (Fig. 7f), suggesting the promising application for one-site producing H<sub>2</sub> and upgrading plastics from seawater.

## 4. Conclusions

In summary, for the first time, the Ni<sub>3</sub>N/W<sub>5</sub>N<sub>4</sub> Janus nanostructure was designed via transition metal nitrides-inducing growth strategy, which was applied as efficient bifunctional catalyst for electrochemical HER and plastics upgrading in seawater. For Ni<sub>3</sub>N/W<sub>5</sub>N<sub>4</sub> hybrid system, the advantages of structure and composition are summarized as the



following aspects: 1) Multilevel nanostructures, which are comprised of 2D  $W_5N_4$  nanosheets and  $Ni_3N$  NPs, and thus expose more active sites and favor the mass transfer process; 2) Barrier-free Janus interface, which not only endows the high electrical conductivity at the hetero-interface but also the excellent ability to resist chloride ion corrosion; 3) Confinement effect of  $W_5N_4$  nanosheets, which largely limits the growth and aggregation of  $Ni_3N$  NPs; 4) Synergistic effect, the  $W_5N_4$  nanosheets exhibiting the super-hydrophilic character and remarkable water dissociation capability, and the  $Ni_3N$  NPs displaying the appropriate  $H^*$  adsorption free energy. Benefiting from the above merits, the  $Ni_3N/W_5N_4$  Janus nanostructure shows commercial Pt-like HER performance, and highly efficient activity toward electro-reforming of plastics waste in deionized water/seawater. This work not only offers a novel method for the construction of multilevel TMNs, but also provides a creative strategy for on-site microplastics disposal and energy-saving  $H_2$  production.

### CRedit authorship contribution statement

**Fahao Ma:** Methodology, Investigation, Writing – original draft. **Shuhua Wang:** DFT calculation. **Xueqin Gong and Xiaolei Liu:** Software. **Zeyan Wang, Peng Wang, Yuanyuan Liu, Hefeng Cheng and Ying Dai:** Funding acquisition, Supervision. **Zhaoke Zheng and Baibiao Huang:** Conceptualization, Writing – review & editing, Funding acquisition.

### Declaration of Competing Interest

The authors declare that they have no known competing financial interests or personal relationships that could have appeared to influence the work reported in this paper.

### Acknowledgements

This work was financially supported by National Key Research and Development Program of China (2020YFA0710301), the National Natural Science Foundation of China (No. 22072072, 21802087, 51972195, 21832005, 22072071 and 21972078), Natural Science Foundation of Shandong Province (ZR2019QB005), Shandong University multidisciplinary research and innovation team of young scholars (2020QNQT11, 2020QNQT012), Qilu Young Scholars and Outstanding Young Scholars Projects of Shandong University, Taishan Scholar Foundation of Shandong Province.

### Appendix A. Supporting information

Supplementary data associated with this article can be found in the online version at doi:10.1016/j.apcatb.2022.121198.

### References

- [1] R. Wei, T. Tiso, J. Bertling, K. O'Connor, L.M. Blank, U.T. Bornscheuer, Possibilities and limitations of biotechnological plastic degradation and recycling, *Nat. Catal.* 3 (2020) 867–871.
- [2] J. Zhu, E.M. Watson, J. Tang, Eugene Y.-X. Chen, A synthetic polymer system with repeatable chemical recyclability, *Science* 360 (2018) 398–403.
- [3] V. Tournier, C.M. Topham, A. Gilles, B. David, C. Folgoas, E. Moya-Leclair, E. Kamionka, M.L. Desrousseaux, H. Texier, S. Gavalda, M. Cot, E. Guemard, M. Dalibey, J. Nomme, G. Cioci, S. Barbe, M. Chateau, I. Andre, S. Duquesne, A. Marty, An engineered PET depolymerase to break down and recycle plastic bottles, *Nature* 580 (2020) 216–219.
- [4] C.-Y. Lin, S.-C. Huang, Y.-G. Lin, L.-C. Hsu, C.-T. Yi, Electrosynthesized Ni-P nanospheres with high activity and selectivity towards photoelectrochemical plastics reforming, *Appl. Catal. B: Environ.* 296 (2021), 120351.
- [5] T. Uekert, H. Kasap, E. Reisner, Photoreforming of nonrecyclable plastic waste over a carbon nitride/nickel phosphide catalyst, *J. Am. Chem. Soc.* 141 (2019) 15201–15210.
- [6] Y. Yang, J. Yang, W.M. Wu, J. Zhao, Y. Song, L. Gao, R. Yang, L. Jiang, Biodegradation and mineralization of polystyrene by plastic-eating mealworms: part 1. chemical and physical characterization and isotopic tests, *Environ. Sci. Technol.* 49 (2015) 12080–12086.
- [7] Q. Hou, M. Zhen, H. Qian, Y. Nie, X. Bai, T. Xia, M. Laiq Ur Rehman, Q. Li, M. Ju, Upcycling and catalytic degradation of plastic wastes, *Cell Rep. Phys. Sci.* 2 (2021), 100514.
- [8] S. Yoshida, K. Hiraga, T. Takehana, I. Taniguchi, H. Yamaji, Y. Maeda, K. Toyohara, K. Miyamoto, Y. Kimura, K. Oda, A bacterium that degrades and assimilates poly (ethylene terephthalate), *Science* 351 (2016) 6278.
- [9] T. Uekert, M.F. Kuehnel, D.W. Wakerley, E. Reisner, Plastic waste as a feedstock for solar-driven  $H_2$  generation, *Energy Environ. Sci.* 11 (2018) 2853–2857.
- [10] F. Zhang, M. Zeng, R. Yappert, J. Sun, Y. Lee, Anne M. LaPointe, B. Peters, Mahdi M. Abu-Omar and Susannah L. Scot, Polyethylene upcycling to long-chain alkylaromatics by tandem hydrogenolysis/aromatization, *Science* 370 (2020) 437–441.
- [11] X. Jiao, K. Zheng, Q. Chen, X. Li, Y. Li, W. Shao, J. Xu, J. Zhu, Y. Pan, Y. Sun, Y. Xie, Photocatalytic conversion of waste plastics into  $C_2$  fuels under simulated natural environment conditions, *Angew. Chem. Int. Ed.* 59 (2020) 15497–15501.
- [12] Y. Nakaji, M. Tamura, S. Miyaoka, S. Kumagai, M. Tanji, Y. Nakagawa, T. Yoshioka, K. Tomishige, Low-temperature catalytic upgrading of waste polyolefinic plastics into liquid fuels and waxes, *Appl. Catal. B: Environ.* 285 (2021), 119805.
- [13] C.M. Pichler, S. Bhattacharjee, M. Rahaman, T. Uekert, E. Reisner, Conversion of polyethylene waste into gaseous hydrocarbons via integrated tandem chemical-photo/electrocatalytic processes, *ACS Catal.* 11 (2021) 9159–9167.
- [14] H. Zhou, Y. Ren, Z. Li, M. Xu, Y. Wang, R. Ge, X. Kong, L. Zheng, H. Duan, Electrocatalytic upcycling of polyethylene terephthalate to commodity chemicals and  $H_2$  fuel, *Nat. Commun.* 12 (2021) 4679.
- [15] H. Zhao, D. Lu, J. Wang, W. Tu, D. Wu, S.W. Koh, P. Gao, Z.J. Xu, S. Deng, Y. Zhou, B. You, H. Li, Raw biomass electroreforming coupled to green hydrogen generation, *Nat. Commun.* 12 (2021) 2008.
- [16] C. Tang, Y. Zheng, M. Jaroniec, S.Z. Qiao, Electrocatalytic refinery for sustainable production of fuels and chemicals, *Angew. Chem. Int. Ed.* 60 (2021) 19572–19590.
- [17] H. Jin, X. Wang, C. Tang, A. Vasileff, L. Li, A. Slattery, S.Z. Qiao, Stable and highly efficient hydrogen evolution from seawater enabled by an unsaturated nickel surface nitride, *Adv. Mater.* 33 (2021), e2007508.
- [18] L. Yu, Q. Zhu, S. Song, B. McElhenny, D. Wang, C. Wu, Z. Qin, J. Bao, Y. Yu, S. Chen, Z. Ren, Non-noble metal-nitride based electrocatalysts for high-performance alkaline seawater electrolysis, *Nat. Commun.* 10 (2019) 5106.
- [19] H. Jin, X. Liu, A. Vasileff, Y. Jiao, Y. Zhao, Y. Zheng, S.Z. Qiao, Single-crystal nitrogen-rich two-dimensional  $Mo_5N_6$  nanosheets for efficient and stable seawater splitting, *ACS Nano* 12 (2018) 12761–12769.
- [20] H. Jin, Q. Gu, B. Chen, C. Tang, Y. Zheng, H. Zhang, M. Jaroniec, S.-Z. Qiao, Molten salt-directed catalytic synthesis of 2D layered transition-metal nitrides for efficient hydrogen, *Evol., Chem.* 6 (2020) 2382–2394.
- [21] J. Cai, Y. Song, Y. Zang, S. Niu, Y. Wu, Y. Xie, X. Zheng, Y. Liu, Y. Lin, X. Liu, G. Wang, Y. Qian, N-induced lattice contraction generally boosts the hydrogen evolution catalysis of P-rich metal phosphides, *Sci. Adv.* 6 (2020) 8113.
- [22] Q. Xu, J. Zhang, H. Zhang, L. Zhang, L. Chen, Y. Hu, H. Jiang, C. Li, Atomic heterointerface engineering overcomes the activity limitation of electrocatalysts and promises highly-efficient alkaline water splitting, *Energy Environ. Sci.* 14 (2021) 5228–5259.
- [23] J. Song, Y.Q. Jin, L. Zhang, P. Dong, J. Li, F. Xie, H. Zhang, J. Chen, Y. Jin, H. Meng, X. Sun, Phase-separated Mo–Ni alloy for hydrogen oxidation and evolution reactions with high activity and enhanced stability, *Adv. Energy Mater.* 11 (2021) 2003511.
- [24] J. Zhu, Y. Guo, F. Liu, H. Xu, L. Gong, W. Shi, D. Chen, P. Wang, Y. Yang, C. Zhang, J. Wu, J. Luo, S. Mu, Regulative electronic states around ruthenium/ruthenium disulfide heterointerfaces for efficient water splitting in acidic media, *Angew. Chem. Int. Ed.* 60 (2021) 12328–12334.
- [25] H. Guo, A. Wu, Y. Xie, H. Yan, D. Wang, L. Wang, C. Tian, 2D porous molybdenum nitride/cobalt nitride heterojunction nanosheets with interfacial electron redistribution for effective electrocatalytic overall water splitting, *J. Mater. Chem. A* 9 (2021) 8620–8629.
- [26] Z. Zhuang, Y. Li, Z. Li, F. Lv, Z. Lang, K. Zhao, L. Zhou, L. Moskaleva, S. Guo, L. Mai, MoB/g-C<sub>3</sub>N<sub>4</sub> interface materials as a schottky catalyst to boost hydrogen, *Evol., Angew. Chem. Int. Ed.* 57 (2018) 496–500.
- [27] Y. Li, X. Tan, H. Tan, H. Ren, S. Chen, W. Yang, S.C. Smith, C. Zhao, Phosphine vapor-assisted construction of heterostructured  $Ni_2P/NiTe_2$  catalysts for efficient hydrogen evolution, *Energy Environ. Sci.* 13 (2020) 1799–1807.
- [28] F. Song, W. Li, J. Yang, G. Han, P. Liao, Y. Sun, Interfacing nickel nitride and nickel boosts both electrocatalytic hydrogen evolution and oxidation reactions, *Nat. Commun.* 9 (2018) 4531.
- [29] F. Lin, Z. Dong, Y. Yao, L. Yang, F. Fang, L. Jiao, Electrocatalytic hydrogen evolution of ultrathin Co-Mo<sub>5</sub>N<sub>6</sub> heterojunction with interfacial electron redistribution, *Adv. Energy Mater.* 10 (2020) 2002176.
- [30] F. Ma, Q. Wu, M. Liu, L. Zheng, F. Tong, Z. Wang, P. Wang, Y. Liu, H. Cheng, Y. Dai, Z. Zheng, Y. Fan, B. Huang, Surface fluorination engineering of NiFe prussian blue analogue derivatives for highly efficient oxygen evolution reaction, *ACS Appl. Mater. Interfaces* 13 (2021) 5142–5152.
- [31] J. Zhang, T. Wang, P. Liu, Z. Liao, S. Liu, X. Zhuang, M. Chen, E. Zschech, X. Feng, Efficient hydrogen production on MoNi<sub>4</sub> electrocatalysts with fast water dissociation kinetics, *Nat. Commun.* 8 (2017) 15437.
- [32] G. Kresse, D.J. Joubert, From ultrasoft pseudopotentials to the projector augmented wave method, *Phys. Rev. B* 59 (1999) 1758.



- [33] G. Kresse, J. Furthmüller, Efficiency of ab-initio total energy calculations for metals and semiconductors using a plane-wave basis set, *Comp. Mater. Sci.* 6 (1996) 15–50.
- [34] G. Kresse, J. Furthmüller, Efficient iterative schemes for ab initio total-energy calculations using a plane-wave basis set, *Phys. Rev.* 54 (1996) 11169.
- [35] J.P. Perdew, K. Burke, M. Ernzerhof, generalized gradient approximation made simple, *Phys. Rev. Lett.* 77 (1996) 3865.
- [36] S. Grimme, J. Antony, S. Ehrlich, H. Krieg, A consistent and accurate ab initio parametrization of density functional dispersion correction (DFT-D) for the 94 elements H-Pu, *J. Chem. Phys.* 132 (2010), 154104.
- [37] J. Paier, R. Hirschl, M. Marsman, G. Kresse, The perdew-burke-ernzerhof exchange-correlation functional applied to the G2-1 test set using a plane-wave basis set, *J. Chem. Phys.* 122 (2005), 234102.
- [38] H. Yu, X. Yang, X. Xiao, M. Chen, Q. Zhang, L. Huang, J. Wu, T. Li, S. Chen, L. Song, L. Gu, B.Y. Xia, G. Feng, J. Li, J. Zhou, Atmospheric-pressure synthesis of 2D nitrogen-rich tungsten nitride, *Adv. Mater.* 30 (2018), e1805655.
- [39] P.R. Jothi, K. Yubuta, B.P.T. Fokwa, A simple, general synthetic route toward nanoscale transition metal borides, *Adv. Mater.* 30 (2018), e1704181.
- [40] H. Park, A. Encinas, J.P. Scheifers, Y. Zhang, B.P.T. Fokwa, Boron-dependency of molybdenum boride electrocatalysts for the hydrogen evolution reaction, *Angew. Chem. Int. Ed.* 56 (2017) 5575–5578.
- [41] B. Liu, B. He, H.Q. Peng, Y. Zhao, J. Cheng, J. Xia, J. Shen, T.W. Ng, X. Meng, C. S. Lee, W. Zhang, Unconventional nickel nitride enriched with nitrogen vacancies as a high-efficiency electrocatalyst for hydrogen evolution, *Adv. Sci.* 5 (2018) 1800406.
- [42] F. Ma, S. Wang, X. Liang, C. Wang, F. Tong, Z. Wang, P. Wang, Y. Liu, Y. Dai, Z. Zheng, B. Huang, Ni<sub>3</sub>B as a highly efficient and selective catalyst for the electrosynthesis of hydrogen peroxide, *Appl. Catal. B: Environ.* 279 (2020), 119371.
- [43] C. Lv, X. Wang, L. Gao, A. Wang, S. Wang, R. Wang, X. Ning, Y. Li, D. W. Boukhvalov, Z. Huang, C. Zhang, Triple functions of Ni(OH)<sub>2</sub> on the surface of WN nanowires remarkably promoting electrocatalytic activity in full water splitting, *ACS Catal.* 10 (2020) 13323–13333.
- [44] A. Wu, Y. Gu, B. Yang, H. Wu, H. Yan, Y. Jiao, D. Wang, C. Tian, H. Fu, Porous cobalt/tungsten nitride polyhedra as efficient bifunctional electrocatalysts for overall water splitting, *J. Mater. Chem. A* 8 (2020) 22938–22946.
- [45] A. Moysiadou, S. Lee, C.S. Hsu, H.M. Chen, X. Hu, Mechanism of oxygen evolution catalyzed by cobalt oxyhydroxide: cobalt superoxide species as a key intermediate and dioxygen release as a rate-determining step, *J. Am. Chem. Soc.* 142 (2020) 11901–11914.
- [46] S. Ibraheem, G. Yasin, A. Kumar, M.A. Mushtaq, S. Ibrahim, R. Iqbal, M. Tabish, S. Ali, A. Saad, Iron-cation-coordinated cobalt-bridged-selenides nanorods for highly efficient photo/electrochemical water splitting, *Appl. Catal. B: Environ.* 304 (2022), 120987.
- [47] Y. Shi, J. Wang, C. Wang, T.T. Zhai, W.J. Bao, J.J. Xu, X.H. Xia, H.Y. Chen, Hot electron of Au nanorods activates the electrocatalysis of hydrogen evolution on MoS<sub>2</sub> nanosheets, *J. Am. Chem. Soc.* 137 (2015) 7365–7370.
- [48] Y. Wu, Y. Xie, S. Niu, Y. Zang, J. Cai, Z. Bian, X. Yin, Y. Fang, D. Sun, D. Niu, Z. Lu, A. Mosallanezhad, H. Wang, D. Rao, H. Pan, G. Wang, Accelerating water dissociation kinetics of Ni<sub>3</sub>N by tuning interfacial orbital coupling, *Nano Res.* 14 (2021) 3458–3465.
- [49] S. Niu, Y. Fang, J. Zhou, J. Cai, Y. Zang, Y. Wu, J. Ye, Y. Xie, Y. Liu, X. Zheng, W. Qu, X. Liu, G. Wang, Y. Qian, Manipulating the water dissociation kinetics of Ni<sub>3</sub>N nanosheets via in situ interfacial engineering, *J. Mater. Chem. A* 7 (2019) 10924–10929.
- [50] D. Si, B. Xiong, L. Chen, J. Shi, Highly selective and efficient electrocatalytic synthesis of glycolic acid in coupling with hydrogen evolution, *Chem. Catal.* 1 (2021) 941–955.